Zeng, G., Shuai, S.S., Zhu, X.Z., Xian, J.W., Gourlay, C.M.

Al_8Mn_5 in High-Pressure Die Cast AZ91: Twinning, Morphology and Size Distributions.

Metallurgical and Materials Transactions A (2020).

https://doi.org/10.1007/s11661-020-05708-1

ACCEPTED MANUSCRIPT

Al_8Mn_5 in high pressure die cast AZ91: twinning, morphology and size distributions

G. Zeng[1,2,*], S.S. Shuai[3], X. Zhu[4], S. Ji[4], J.W.Xian[2] and C. M. Gourlay[2*].

[1]School of Materials Science and Engineering, Central South University, Changsha 410083, China
[2]Department of Materials, Imperial College London, London, SW7 2AZ, UK
[3]State Key Laboratory of Advanced Special Steel, School of Materials Science & Engineering, Shanghai University, 200444, Shanghai, China
[4] BCAST, Institute of Materials & Manufacturing, Brunel University London, Uxbridge, UB8 3PH, UK

* corresponding authors: g.zeng@csu.edu.cn and c.gourlay@imperial.ac.uk

Abstract

Manganese-bearing intermetallic compounds (IMCs) are important for limiting micro-galvanic corrosion of magnesium-aluminium alloys and can initiate cracks under tensile load. Here we use electron backscatter diffraction (EBSD), deep etching, and focussed ion beam (FIB) tomography to investigate the types of Al-Mn phases present, their faceted growth crystallography, and their three-dimensional distribution at different locations in high pressure die cast (HPDC) AZ91D. The Al-Mn particle size distributions were well-described by lognormal distributions but with an additional population of externally solidified crystals (ESCs) formed in the shot chamber analogous to α-Mg ESCs. The large Al_8Mn_5 particles were cyclic twinned. Differences in the particle size distributions and number density in the centre compared with the HPDC skin are identified, and the spatial relationship between $Mg_{17}Al_{12}$ and Al-Mn particles is explored.

Keywords AZ91, high pressure die casting, intermetallics

Introduction

Automotive magnesium components are often Mg-Al-based alloys produced by high pressure die casting (HPDC). When conducted with an optimised die, process parameters and vacuum system [1,2], HPDC can mass produce large, thin-walled, complex shapes containing microstructures with fine α-Mg grains (5-20 μm) [3,4], and a fine-scaled percolating eutectic $Mg_{17}Al_{12}$ network [5,6]. While a large body of research has investigated microstructure formation in Mg HPDC, including the formation of α-Mg grains [3,4,7], the surface 'skin' [4,8], the eutectic $Mg_{17}Al_{12}$ [5,9,10], and casting defects [11–17], less work has explored the formation of Al-Mn-(Fe) intermetallic particles [18–21]. These particles play an important role in determining micro-galvanic corrosion in HPDC Mg parts [22,23] and can initiate cracks under tensile loading [24,25].

Most Mg-Al-based HPDC alloys (e.g. AM50A, AM60B, AZ91D [26]) contain sufficient Mn and Al that Al_8Mn_5 begins to form before α-Mg during solidification. For example, Figure 1 shows the sequence of phase formation assuming Scheil solidification of AZ91D with the composition in Table 1, calculated with the Thermo-Calc TCMG magnesium database version 4 [27]. It can be seen that Al_8Mn_5 is the first solid phase to form, and becomes stable ~44K above the α-Mg liquidus temperature for this composition. It has been confirmed by in-situ X-ray imaging that Al_8Mn_5 forms at higher temperature (i.e. earlier on cooling) than α-Mg in a similar alloy [28,29]. A consequence of this in HPDC is that Al_8Mn_5 can form and settle in the holding pot [29,30], for example during temperature drops when charging the furnace with new ingots, leading to die casting sludge [30]. Furthermore, in cold chamber HPDC, heat loss in the shot chamber can cause Al_8Mn_5 formation prior to injection as Al_8Mn_5 externally solidified crystals (ESCs) [20] in addition to the α-Mg ESCs that are widespread in HPDC Mg components [3,14,31]. This occurs because a feature of Mg HPDC is partial solidification in the shot chamber that leads to large α-Mg externally solidified crystals (ESCs) being injected into the cavity [3,32]. The volume fraction of α-Mg ESCs has been shown to depend on the melt superheat, the fill fraction and the temperature of the sleeve walls and plunger tip, and is typically 10-30 vol.% [3,14,31,33]; similar factors might be expected to determine the formation of Al_8Mn_5 ESCs.

Table 1. Composition of the AZ91D alloy used (weight percent).

Mg	Al	Zn	Mn	Fe	Ni	Cu	Si	Be
bal.	8.95	0.72	0.19	<0.001	<0.001	0.001	0.039	0.0007

Figure 1 shows that Al_8Mn_5 continues forming along with α-Mg below the α-Mg liquidus temperature until ~ 510°C when other Al-Mn IMCs start forming ($Al_{11}Mn_4$ and then Al_4Mn). Therefore, in HPDC, Al-Mn IMCs are expected to form in all stages of the process: in the shot chamber, during filling and during the intensification stage. According to calculations linked with Figure 1, at the end of Scheil solidification, the total mass fraction of Al-Mn IMCs (Al_8Mn_5, $Al_{11}Mn_4$ and Al_4Mn) is 0.25% of which 95% is Al_8Mn_5 for the composition in Table 1.

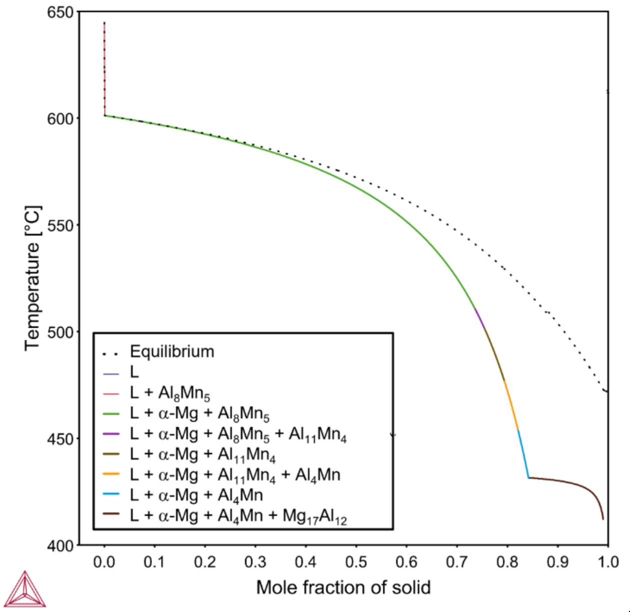

Figure 1: Phase formation during Scheil solidification up to 99% solid for Mg-8.95Al-0.72Zn-0.19Mn (wt%). Calculated with Thermo-Calc TCMG magnesium database version 4 [27].

Past work on Al-Mn particles in HPDC AZ91D has generally used TEM [18,19,21]. That work has deduced that most Al-Mn particles in HPDC AZ91D are 100 nm to 1μm in size. The main phase present has been found to be Al_8Mn_5 and another phase with higher Al content (possibly $Al_{11}Mn_4$) has also been reported [18]. While these TEM studies enable high resolution imaging, they did not explore the statistical variation in Al-Mn particle size and shape versus position in the cross-section. This is an important question in HPDC parts since they usually have highly non-uniform microstructures. They typically have a surface layer (a skin) of distinctly different microstructure that is usually free of porosity and harder than more central regions, one or more bands of porosity, various forms of macrosegregation, and ESCs that tend to be concentrated towards the centre of cross-sections (e.g. [15,16,33,34]).

In this paper, we investigate the types of Al-Mn phases present, their faceted growth crystallography, and their three-dimensional distribution at different locations in high pressure die cast AZ91D. The specific aims are: (i) to compare the Al_8Mn_5 growth crystallography and twinning formed in HPDC with past work at sand casting cooling rates [35]; (ii) to quantify the 3D size, morphology and spatial distribution of Al-Mn particles in different locations in HPDC AZ91D: the skin, the defect band, and the centre; and (iii) to explore any correlations between Al-Mn particles and eutectic $Mg_{17}Al_{12}$ in 3D.

Methods

~6 kg of AZ91D Mg alloy with composition in Table 1 was melted in a mild steel crucible and held at 675°C (~ 75°C superheat) under a cover gas of ~3 vol% SF_6 in N_2. HPDC was conducted using a Frech DAK 450-54 cold chamber HPDC machine and the multi-cavity die that produces the casting in Figure 2. The die was preheated to 150°C, a portion of the melt was ladled into the shot chamber to a fill fraction of ~0.5, and the following set parameters were used: slow shot phase of 0.3 $m.s^{-1}$, fast shot phase of 4 $m.s^{-1}$, and intensification pressure of 36 MPa. The casting analysed in this work was made after six pre-shots.

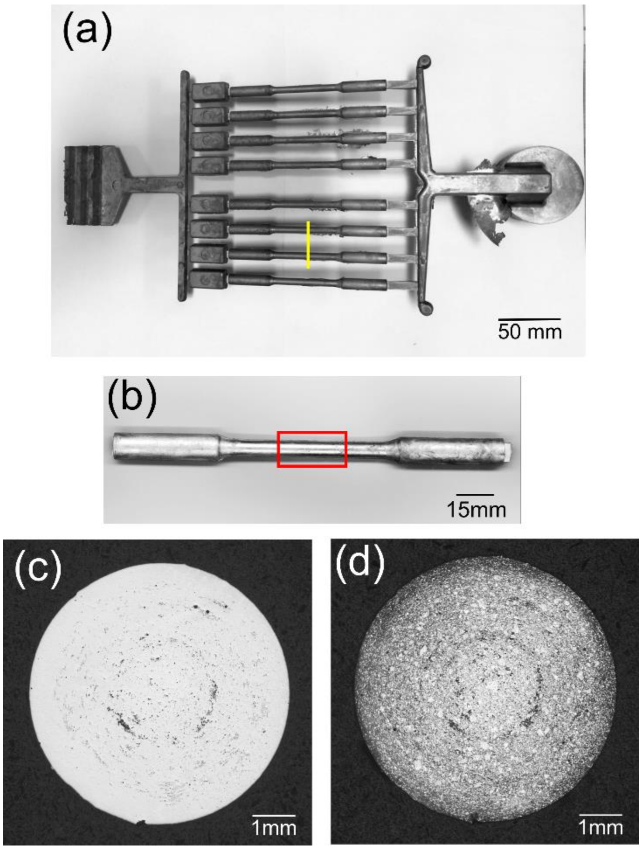

Figure 2 (a-b) Photographs of the HPDC part. The sectioning plane is indicated by superimposed lines. (c) as-polished optical micrograph.(d) the same section after etching.

Samples for microstructural analysis were cut from the centre of the gauge length into slices of 10mm x 10mm x 0.5mm. Metallographic polishing was carried out down to 0.05μm colloidal silica by standard preparation methods. Some samples were etched in a solution of 200ml ethylene glycol, 68ml distilled water, 4ml nitric acid and 80 ml acetic acid. Both etched and polished samples were analysed in a Zeiss AURIGA field emission gun SEM (FEG-SEM) with an Oxford Instruments INCA x-sight energy dispersive X-ray spectroscopy (EDX) detector and a BRUKER e-Flash^{HR} electron backscatter diffraction (EBSD) detector. For EBSD characterisation, the final step of preparation was Ar-ion milling for 40 min in a Gatan PECSII instrument. The 4 kV-accelerated beam hit the sample rotating at 2 rpm, at a grazing incidence angle of 4°. Electron beam accelerating voltage of 20kV, working distance of 15mm, aperture size of 120mm, and beam current 80μA were used for EBSD measurements. Bruker ESPRIT 2.1 software was used to index the obtained EBSD patterns. EBSD datasets were analysed using MATLAB™ 9.2 (Mathworks, USA) with the MTEX 5.1 toolbox [36]. Accelerating voltage of 10kV, working distance of 5mm, aperture size of 60mm, and beam current 80μA were used for EDS analysis. EDS spectrum was calibrated with a Si standard sample prior to each electron microscopy session.

To investigate the 3-dimensional (3D) morphology of the Al-Mn intermetallics directly, α-Mg was selectively etched using a solution of 4% nitric acid in ethanol. To quantify the 3D size distribution of Al-Mn intermetallics, focussed ion beam (FIB) tomography was conducted in a Zeiss AURIGA FG-SEM at 30 kV with 52° tilt angle. The slice distance was 90 nm and the milling current was 200pA. Serial-sectioning secondary electron images were used. For FIB tomography, 2D slices were aligned, cropped, and processed by an anisotropic diffusion filter in ImageJ (US NIH, USA). 3D reconstruction and crystallographic analysis was performed using Avizo 9.2 (Visualization Science Group, France) and MATLAB 9.2™. The voxel size for FIB tomography was bounded by the slice spacing of 90nm. Al_8Mn_5 particles with equivalent diameter ≧ 180nm were quantified.

To study porosity bands in 3D, X-ray micro-tomography was carried out on a North Star Imaging (NSI) Micro-CT. The system is equipped with a 225 kV X-ray source with a minimum focal spot size of 2 μm and a Perkin Elmer flat panel detector (2048×2048 pixels at 16bit depth). During a CT scan, the sample was illuminated by cone beam X-rays which were transmitted through the 360° rotating specimen and then illuminated on the flat panel detector. The X-ray beam was filtered using a 0.25 mm Cu filter to reduce beam-hardening effects, and an acceleration voltage of 80kV and target current of 35μA was selected to optimise image quality. 1440 two-dimensional projections were captured over 360° with an exposure time of 1000ms. 3D reconstruction was performed in Avizo 9.2 and resulted in a 3D spatial resolution with voxel size of 2.2 μm x 2.2 μm x 2.2 μm.

3 Results and Discussion

3.1 General microstructural features

At the centre of the gauge length, the AZ91D samples contained the typical microstructural features and defects of HPDC reported in past work (e.g. [3,7,12,14,16,33,34,37]). For example, annular rings of porosity can be seen in the as-polished condition in Figure 2(c), a dark band of macrosegregation can be seen in the same location as the main porosity band in Figure 2(d) after light etching, and a high fraction (~30 vol%) of α-Mg ESCs can be seen throughout much of the cross-section in Figure 2(d). However, the detail of these features differed significantly from casting to casting and between bars in the same casting as shown in the X-ray tomographs in Figure 3. The left-hand images are reconstructed volumes near the centre of the gauge length showing the 3D distribution of porosity. The right-hand images are viewed along the tensile rod axis to highlight the radial distribution of porosity. There are major differences in the porosity in the two samples. The sample in Figure 3(b) has a localised annular ring of porosity and a high fraction of porosity within this ring. The sample in Figure 3(a) has more diffuse porosity and a less-well defined porosity ring but has the same trend of a higher fraction of porosity within the annular porosity band. Despite the differences, in both samples, the main annular ring of porosity is at a similar radial position. The projection images along the rod axes also reveal the surface 'skin' as an outer ring of essentially zero porosity. This is particularly clear in Figure 3(a) where the abrupt change in porosity demarcates the edge of the skin.

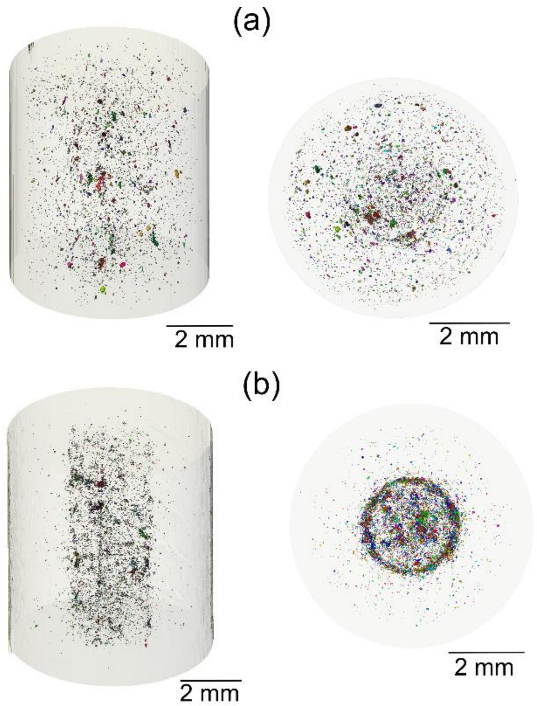

Figure 3 (a-b) X-ray tomograms of porosity near the centre of the gauge-length of typical castings. Porosity is rendered as solid, material (Mg, $Mg_{17}Al_{12}$ and Al-Mn IMCs) is plotted as semi-transparent. Left-hand side: perspective view. Right-hand side: projection view along the tensile rod axis.

The typical α-Mg microstructure is shown in more detail in Figure 4(a)-(b). The micrograph in Figure 4(a) shows the complex mixture of dendritic α-Mg ESCs, ESC fragments and in-cavity solidified grains. Figure 4(b) is an EBSD orientation map (IPF-y) of the α-Mg phase from a similar region where the grains have been coloured by their mean-orientation. The grains form a complex multimodal microstructure with, in this case, two large ESCs surrounded by smaller α-Mg grains that are probably a mixture of α-Mg ESC fragments and in-cavity solidified grains.

The typical features of intermetallic compounds in the HPDC bars are overviewed in Figure 4(c) and (d). It can be seen that the eutectic $Mg_{17}Al_{12}$ phase appears as isolated regions in 2D sections (Figure 4(c)) but actually forms a percolating $Mg_{17}Al_{12}$ network in 3D as revealed by imaging after selective dissolution of the α-Mg in Figure 4(d). Figure 4(c) and (d) also contains bright particles that are Al-Mn compounds. In the 2D section these appear both within the α-Mg grains and near the $Mg_{17}Al_{12}$ phase (Figure 4(c)). After deep etching, it can be seen that many Al-Mn particles are attached to the $Mg_{17}Al_{12}$ network (Figure 4 (d)).

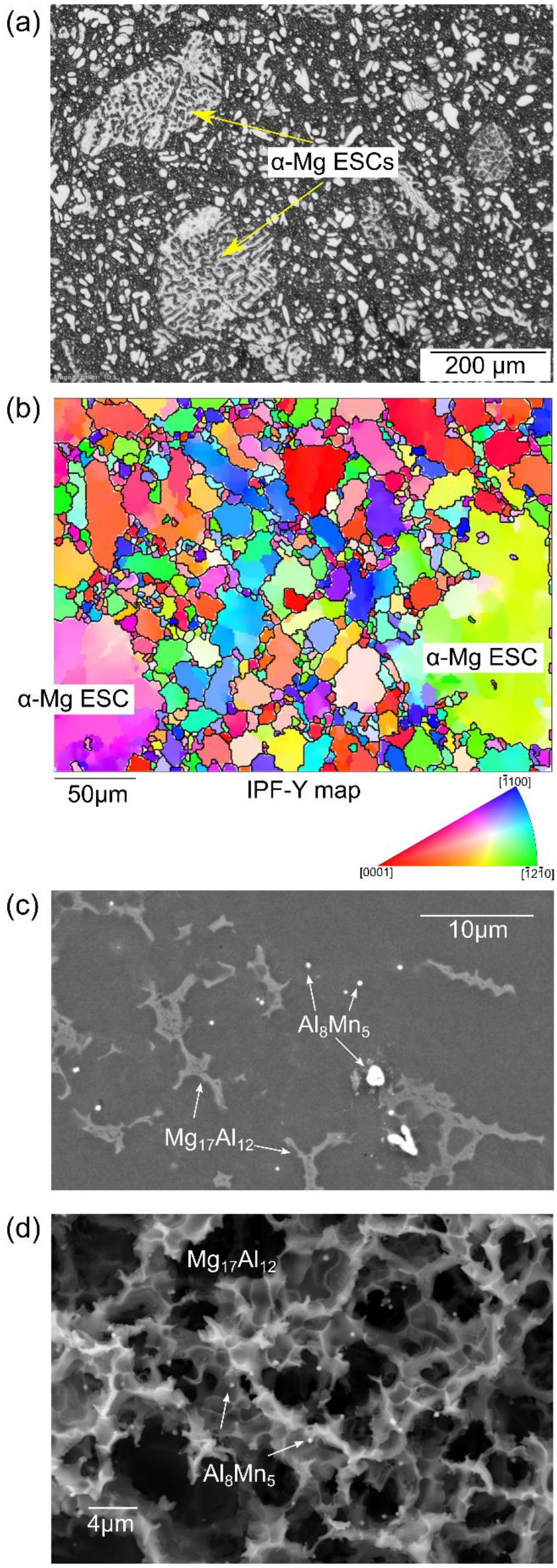

Figure 4: Typical microstructural features in the HPDC AZ91 samples. (a) mixture of α-Mg ESCs and in-cavity solidified grains. (b) EBSD orientation map (IPF-Y) of the α-Mg phase. (c) 2D section of $Mg_{17}Al_{12}$ and Al_8Mn_5 phases. (d) 3D microstructure of $Mg_{17}Al_{12}$ network and attached Al_8Mn_5 particles, revealed after selective etching of α-Mg .

The remainder of this paper focuses on the Al-Mn intermetallic compounds and their relationship to the microstructural features summarised in this section.

3.2 Twinned Al_8Mn_5 in HPDC AZ91D

Al-Mn intermetallics were identified by combining EDS with EBSD. A typical EDS point analysis from an Al-Mn particle is shown in Figure 5(a). The particle contains 59at%Al - 40at%Mn and there are also small Mg, Si and Fe peaks, each present at less than 1 at%. Since the solubility of Mg in Al-Mn intermetallics is negligible [38], the small Mg peak is likely to be α-Mg in the interaction volume. The small Si peak is probably Si dissolved in the particle, consistent with past work that has detected a small Si content in Al-Mn IMCs [18,39]. The low Fe content in the particle is due to the high-purity AZ91D used in this study (with <10ppm Fe, Table 1).

An EBSD pattern from the Al-Mn particle is shown in Figure 5(b). This could be readily distinguished as the rhombohedral Al_8Mn_5 phase [40,41] using the Hough transform-based method in Bruker ESPRIT 2.1, and is indexed in Figure 5(c) in the hexagonal setting R3mH. Although various Al-Mn intermetallics are known to exist and three are expected to form (Al_8Mn_5, $Al_{11}Mn_4$ and Al_4Mn) according to Scheil calculations using current thermodynamic databases [27], the strong crystallographic differences between these phases enabled Al_8Mn_5 to be clearly distinguished. Al_8Mn_5 is also consistent with the EDS measurement of 59at%Al - 40at%Mn. Note that rhombohedral Al_8Mn_5 is also known as γ_2 [42] and LT-AL_8Mn_5 [43] , and is a gamma brass with Strukturbericht designation $D8_{10}$. It is useful to index this crystal structure in the non-standard body-centred rhombohedral (BCR) setting as discussed in refs. [35,41,44].

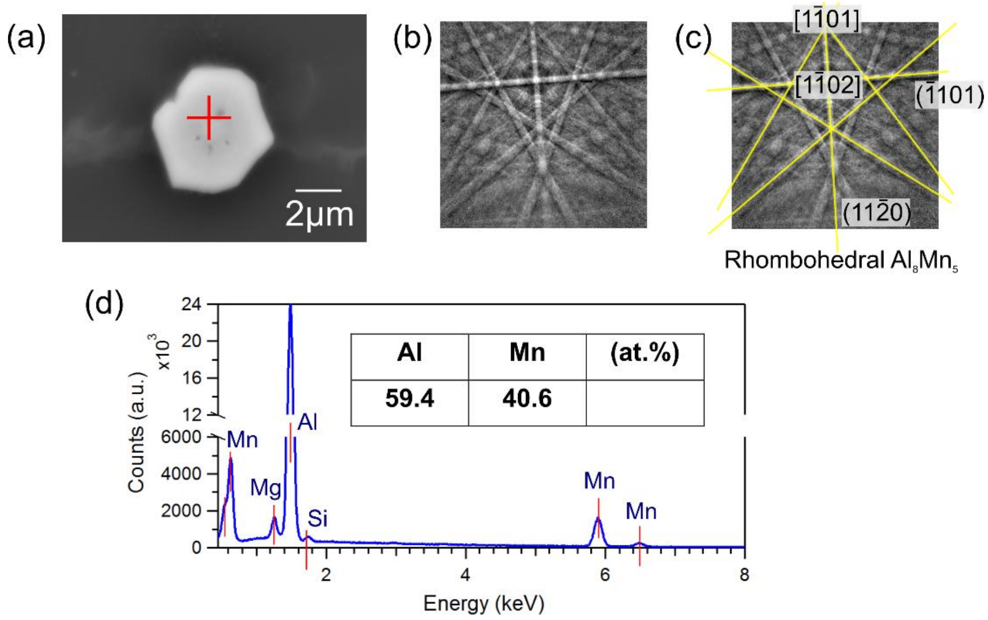

Figure 5: (a) EDS spectrum from the particle in (b). (c) EBSD pattern from the same particle. (d) EBSD pattern indexed as rhombohedral Al_8Mn_5 ($D8_{10}$).

Rhombohedral Al_8Mn_5 was the only Al-Mn intermetallic detected in the HPDC AZ91D samples by SEM-based techniques in this work. This is reasonably consistent with Scheil calculations within Thermo-Calc Software TCMG magnesium database version 4 [27] which show that ~95% of all the Al-Mn phases formed during Scheil solidification are Al_8Mn_5 (using the composition in Table 1). If $Al_{11}Mn_4$ and/or Al_4Mn were present in the HPDC samples, they were either too low in volume fraction or too small to be detected. The B2-Al(Mn,Fe) phase identified in AZ91 in ref. [35] was not detected in this work, most likely because the AZ91 used here (Table 1) had a very low Fe content (<10 ppm).

It was found that most HPDC Al_8Mn_5 particles were cyclic twinned containing up to four orientations, similar to the Al_8Mn_5 particles at low cooling rate identified in ref. [35]. For example, Figure 6(a) is a typical ~5 μm HPDC Al_8Mn_5 particle and Figure 6(b) is its EBSD orientation map showing the presence of three orientations within the particle. Note that the grey pixels have unknown orientation due to low EBSD pattern quality in this region. The three orientations are plotted in pole figures in Figure 6(c) which show that all three orientations share three common $\{100\}_{BCR}$ planes and each orientation shares a common $\{110\}_{BCR}$ plane with one of the other orientations. This orientation relationship between the three Al_8Mn_5 orientations is shown geometrically in Figure 6(e) which is a plot of the BCR unit cell wireframes using the EBSD-measured Euler angles and coloured consistent with Figure 6(b)-(c). The green orientation was not measured experimentally for this 2D section of the particle but is likely to be present in the 3D particle based on the findings in our previous work [35]. Note that the BCR unit cell of Al_8Mn_5 has rhombohedral angle ~89° [40,41] and so appears as near-cubes in Figure 6(e). Figure 6(f) is a digital section through the geometrical model in Figure 6(e). It can be seen that the Al_8Mn_5-Al_8Mn_5 interfaces in the sliced BCR model have similar angular arrangement with the experimental interfaces in Figure 6(b), consistent with the interfaces being $\{100\}_{BCR}$. The cyclic growth twinning of Al_8Mn_5 with $\{100\}_{BCR}$ twin planes can be understood by noting that, with a rhombohedral angle of ~89° [40,41], the crystal is pseudo-cubic which gives the possibility for growth twins with $\{100\}_{BCR}$ interfaces by ~90° rotations around the three $<100>_{BCR}$ axes [35].

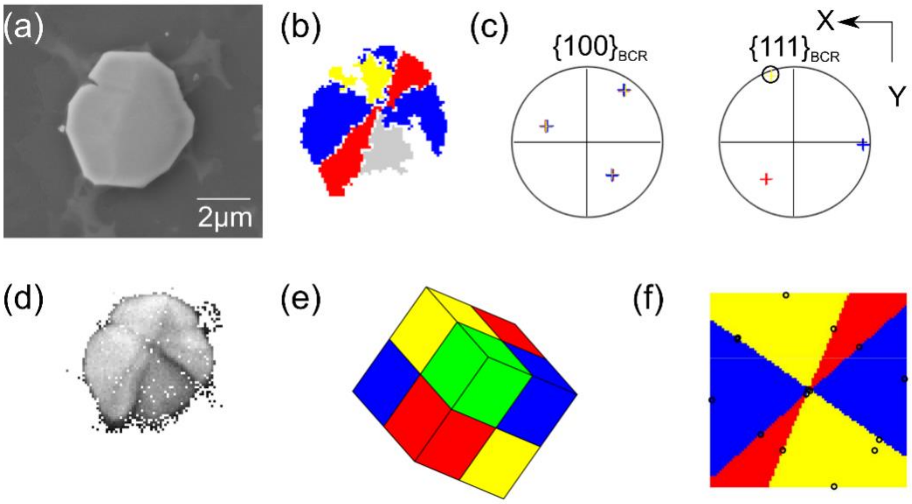

Figure 6. Cyclic growth twinning of Al_8Mn_5 particles in HPDC AZ91. (a) SEM image, (b) EBSD orientation map in RGBY colour scheme,(Grey region has unknown orientation due to low pattern quality). (c) $\{100\}_{BCR}$ and $\{111\}_{BCR}$ pole figures showing the three orientations. (d) band contrast map showing grain boundaries. The three BCR unit cell orientations (plus a green orientation that was not present in the cross-section). (f) $\{100\}_{BCR}$ twin planes revealed by sectioning the BCR geometrical model.

In the HPDC AZ91D sample studied here, it was found that all equiaxed polyhedral Al_8Mn_5 particles that were large enough for EBSD mapping were cyclic twinned. Comparing Figure 6 in this paper with the TEM images in Fig. 4(a) in ref [19] and Fig. 7(b) in ref. [21], it is likely that the HPDC Al_8Mn_5 particles in references [19,21] contain sector-twins and were also cyclic twinned, although those authors did not study or mention this.

Having confirmed that the majority of Al-Mn particles are Al_8Mn_5 by combined EDS and EBSD, Al_8Mn_5 could be distinguished in backscattered electron (BSE) images due to the much higher atomic-number of Mn compared with Mg and Al. For example, in Figure 2(c), the numerous bright particles are Al_8Mn_5 and the lighter grey particles are $Mg_{17}Al_{12}$.

3.3 Al_8Mn_5 morphologies

The HPDC AZ91D bars contained a range of Al_8Mn_5 morphologies that could be broadly classified into two categories: equiaxed-polyhedral and complex-branched particles. A representative selection is shown in Figure 7 where Figure 7(a) are equiaxed-polyhedral morphologies, and Figure 7(b) are a range of complex-branched morphologies. Each column represents a different location in the test bars: the centre of the cross-section, the defect band, and the skin. It can be seen that similar morphologies were present at each location of the castings, although the size distributions were different as will be discussed in detail later in this paper.

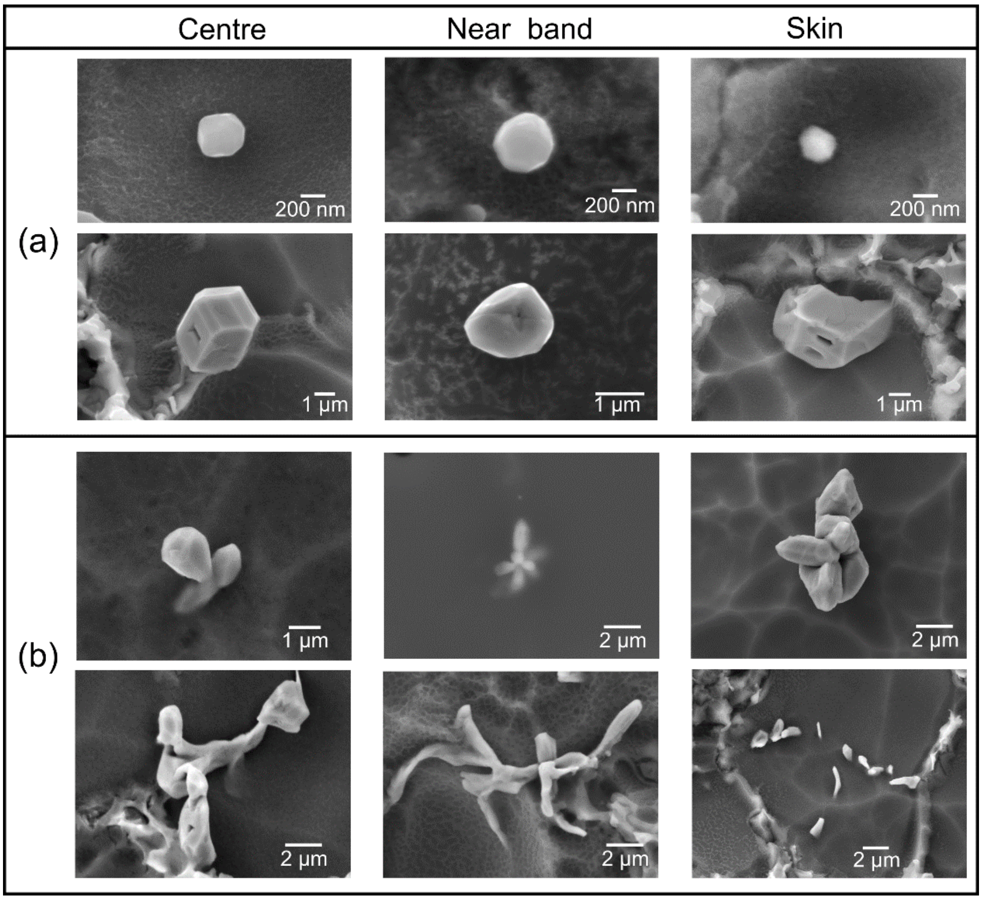

Figure 7: Typical range of Al_8Mn_5 morphologies in one HPDC AZ91 sample. SE-SEM images after selective etching of the α-Mg. (a) equiaxed polyhedral particles, (b) complex branched particles.

It has been shown by in-situ X-ray imaging of AZ91 solidification at low cooling rate [28,29], that the Al_8Mn_5 particles that form in the early stages of solidification are equiaxed polyhedral and it is likely, therefore, that the equiaxed-polyhedral particles in these HPDC samples also formed in the earlier stages of solidification. The complex-branched particles in the bottom row of Figure 7(b) may have formed relatively late during a eutectic-type reaction when the remaining liquid regions were tortuous channels. This is consistent with Figure 1 which shows that, for Scheil solidification, Al_8Mn_5 forms both as a primary phase prior to α-Mg formation (the red line) and also by a eutectic-type reaction with α-Mg (the green line), $L \rightarrow \alpha\text{-Mg} + Al_8Mn_5$, over a range of temperature up to ~70% solid. However, further work is required to confirm that the complex-branched particles in the bottom row of Figure 7(b) formed in this eutectic-type reaction.

Past work on investment cast AZ91 reported dendritic Al_8Mn_5 near the surface [45]. In the HPDC samples studied here, the complex-branched particles occasionally had dendritic morphology (e.g. some in the top row of Figure 7(b)) but these were present at all locations in the casting. FIB serial sectioning on one branched-faceted Al_8Mn_5 crystal with morphology similar to the top row of Figure 7(b) was conducted to explore its formation. The FIB slices confirmed that, in this case, the branched structure grew from a common centre. At the same time, it is also possible that other complex-branched Al_8Mn_5 similar to the top row of Figure 7(b) are clusters of equiaxed-polyhedral particles that were swept together during solidification.

3.4 Al_8Mn_5 externally solidified crystals (ESCs)

The Al_8Mn_5 particles had a wide range of sizes spanning from <100 nm to >5μm, which is significantly broader than in previous work at sand-casting cooling rates. For example, in ref. [35], the Al_8Mn_5 particle size varied from 4-14 μm for a cooling rate of ~1 $K.s^{-1}$. Figure 8(a) is a typical micrograph of a region containing Al_8Mn_5 particles with a wide size range in the HPDC samples. A ~4μm Al_8Mn_5 particle can be seen that is an order of magnitude larger than the numerous smaller Al_8Mn_5 particles in the surrounding material. It is likely that the large particle is an Al_8Mn_5 ESC that nucleated and grew in the shot chamber at low cooling rate before being injected into the die cavity analogous to the α-Mg ESCs in Figure 2(d) and 4(a)-(b), whereas the smaller Al_8Mn_5 nucleated and grew at higher cooling rate. This can be concluded based on three factors: (i) the larger (~5 μm) Al_8Mn_5 particles in (e.g. Figures 5(a), 6(a) and 8(a)) are within the range of Al_8Mn_5 particle sizes reported for a cooling rate of ~1 $K.s^{-1}$ in past work [35], indicating that they did not form in the die cavity at high cooling rate; (ii) as will be shown in the next section, the larger (~5 μm) Al_8Mn_5 particles do not belong to the same population as the smaller Al_8Mn_5 particles and the Al_8Mn_5 exhibit a multi-model grain size distribution similar to α-Mg grains in HPDC parts containing α-Mg ESCs (e.g. [3]); and (iii) Al_8Mn_5 ESCs are expected since these samples contain α-Mg ESCs (Figure 4) and Al_8Mn_5 is stable above the α-Mg liquidus (Figure 1) for the composition in Table 1 [27]. Note that abnormally large Al_8Mn_5 particles in HPDC parts can be even larger, with a 20μm Al_8Mn_5 particle found in HPDC AM50 in ref. [20].

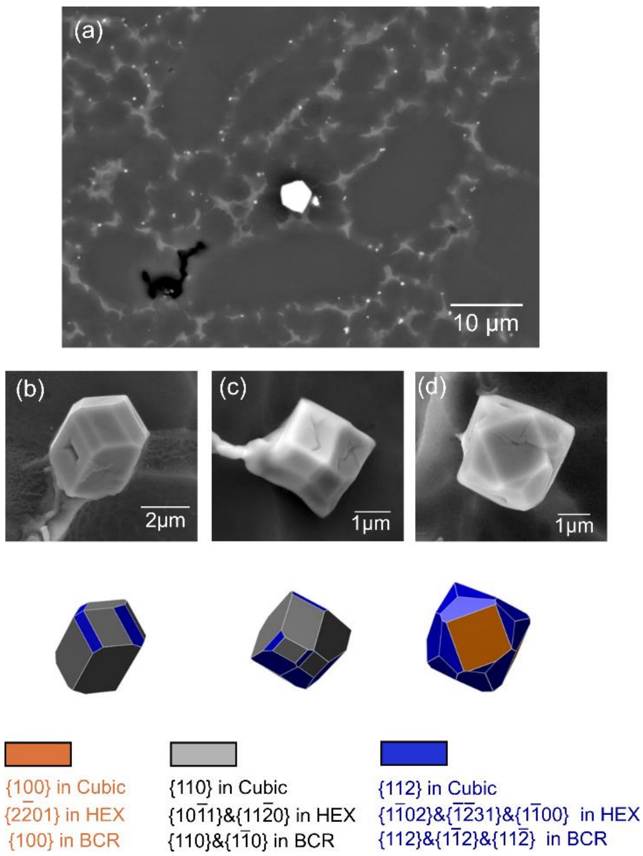

Figure 8: (a) a typical large Al_8Mn_5 particle in HPDC AZ91D. (b-d) SE-SEM images of three Al_8Mn_5 particles after selective etching of α-Mg, and polyhedron models based on {100}, {110}, {112} facets using a pseudo-cubic cell.

In our previous work at sand-casting cooling rates [35], we identified the Al_8Mn_5 growth facets using combined FIB-EBSD techniques as combinations of {100}, {110} and {112} using a pseudo-cubic (pc) BCR unit cell. To explore whether the larger Al_8Mn_5 particles in these HPDC samples had similar growth facets, deep etched images of Al_8Mn_5 particles were explored using polyhedron models. It was found that the deep etched images could usually be recreated from combinations of $\{100\}_{pc}$, $\{110\}_{pc}$ and $\{112\}_{pc}$ facets. Three such examples are shown in Figure 8(b)-(d) where the models were generated by plotting the {100}, {110} and {112} cubic facet families, and tuning the distance from the centroid to each facet to best match the deep etched SEM images. Thus, the larger Al_8Mn_5 particles in HPDC AZ91D have similar facets to sand cast AZ91 [35].

The wide range of polyhedral Al_8Mn_5 forms based on different combinations of the facet families indicates that these growth facets are sensitive to the local solidification conditions (thermal, solutal and/or kinetic) which are expected to vary substantially with time and location in the HPDC process. No simple trend of the polyhedral form of Al_8Mn_5 versus location in the HPDC part was identified in this work.

3.5 3D size distributions of Al_8Mn_5 particles

Figure 9(a) shows typical 3D rendered images of Al_8Mn_5 particles from FIB tomography with a 50nm slice step size. Each volume is ~13x13x13 μm^3 and comes from one of three locations: the casting centre, the porosity band, and the skin. Figure 9 (b) show histograms of the Al_8Mn_5 particle size distribution at each location. The histograms contain data from multiple tomograms as summarised in Table 2. The size distributions are plotted in terms of the number of Al_8Mn_5 particles and in terms of the volume occupied by the Al_8Mn_5 particles, separately. Two definitions of Al_8Mn_5 particle size are used: the equivalent sphere diameter and the "3D length". The latter is defined as the longest Feret diameter. Note in Figure 9(a) that the rendering causes the Al_8Mn_5 particles to appear rounded, but the particles are actually faceted as can be seen in the typical images from FIB sectioning shown as insets in the histograms of Figure 9(b). The volume fraction of Al-Mn IMCs varied from 0.11-0.22 vol. % depending on the location (Table 2). This is similar to the 0.10 vol.% calculated with Thermo-Calc TCMG4.0 [27] for the composition in Table 1, and 0.18% measured by Wang et al. [46] for HPDC AZ91D, which shows that a sufficient volume of material has been sampled and the thresholding approach was reasonable. The particle size results in Figure 9 are in general agreement with past work using TEM on small volumes. For example, Wei et al. [18] reported that Al-Mn particles were 100 nm to ~ lμm and usually less than 500 nm in AM and AZ Mg HPDC parts, and Wang et al. [19] reported Al_8Mn_5 to have polygonal morphology with size about 100 - 200 nm in HPDC AZ91D.

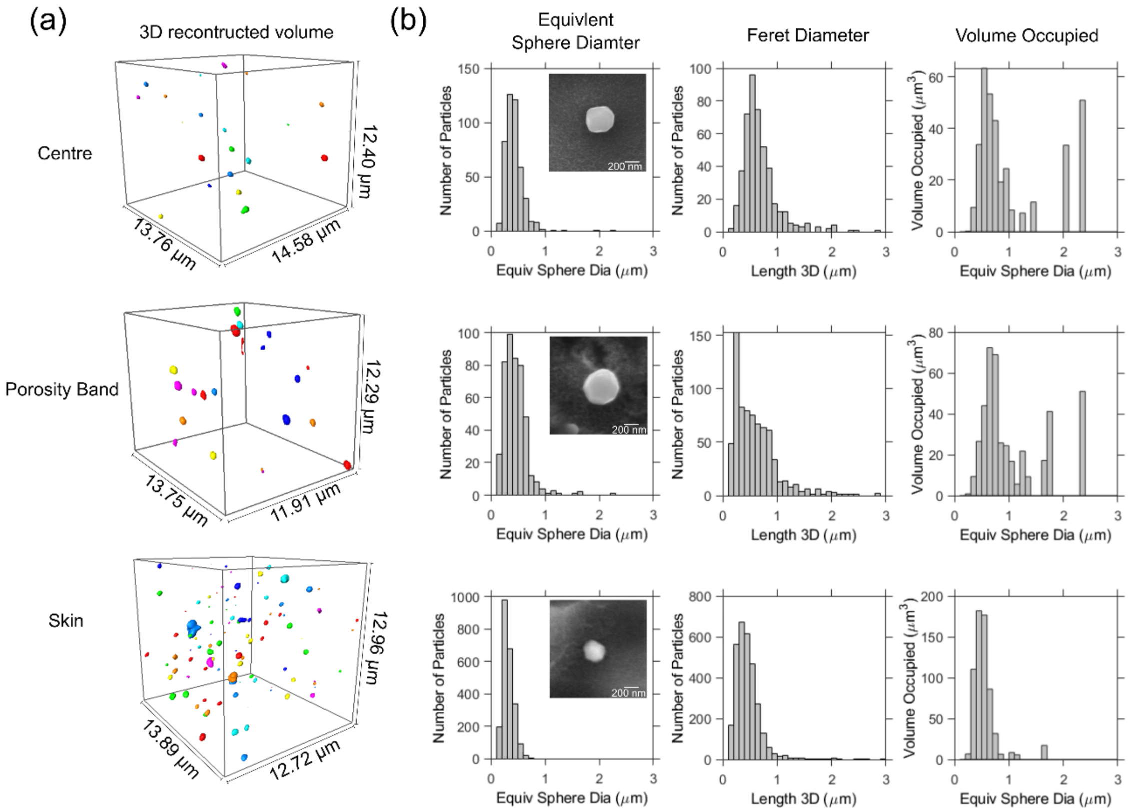

Figure 9: Al_8Mn_5 particle size data in different locations in the HPDC cross-section based on FIB-tomography. (a) Rendered images of Al_8Mn_5 particles in volumes of ~13x13x13 μm^3. Each particle has a unique colour. (b) Al_8Mn_5 particle size histograms in terms of the number of particles and the volume occupied by particles. The inset micrographs are typical 2D SEM images of Al_8Mn_5 particles in each location. The scale bar is 200nm in each case.

Table 2: Summary of the Al_8Mn_5 particle size data at different locations in HPDC AZ91D extracted from the distributions in Figs. 9 and 10 from FIB-tomography. ESD= equivalent sphere diameter. IMC= intermetallic compound. (ESD>180nm particles calculated)

		Center	Band	Skin
Distance from surface	[μm]	2700-2900	1500-1600	10-20
Number of tomograms	[-]	6	3	4
Total volume sampled	[μm^3]	24726	40203	25660

Number of IMCs measured	[-]	449	451	6547
Mean ESD	[nm]	432	453	163
Median ESD	[nm]	408	421	99.2
Standard deviation in ESD	[nm]	189	219	133
Maximum ESD	[nm]	2245	2245	1534
Volume of all Al-Mn IMCs	[μm^3]	35.9	44.3	55.8
Number density of particles	[μm^{-3}]	0.0182	0.0112	0.2551
Volume Fraction of IMCs	[-]	0.0015	0.0011	0.0022

The distributions are analysed in more detail in Figure 10 and summarised in Table 2. Figure 10(a) are box plots showing the median, the 25th percentile and 75th percentile, and a significant tail at large size in each particle population. Note that the largest Al_8Mn_5 particle in Figure 10(a) and Table 2 is less than 2.3μm, which is significantly smaller than the Al_8Mn_5 particle in Figure 5(b), 6(a) and 8(a) (>4μm), so the tail to large size extends to even larger size than in Figure 10(a), even though the randomly-selected regions only contained particles up to ~2.3μm.

The particle size distribution data were compared with various distributions including normal, lognormal and Weibull using probability test plots. At each location, the data were best described by a lognormal distribution as shown in Figure 10(b). This is consistent with many past studies that have shown grain size and particle size distributions are often well-described by a lognormal distribution (e.g. [3,47]) including Fe-bearing IMCs in cast aluminium alloys [48,49]. In Figure 10(b), there is a negative deviation from the lognormal test line at large particle size and at small particle size. At small size (<~200nm) this might be, at least partly, due to measurement uncertainty caused by the 50nm FIB slice distance. At large particle size (>~1 μm at a cumulative probability >~99%), the negative deviation from the straight line corresponds to Al_8Mn_5 particles larger than expected of this lognormal population. The presence of this small number of abnormally large grains in the populations can also be seen in the volume occupied histograms in Figure 9(a), especially at the casting centre and near the defect band. From this, and the observation of many abnormally large Al_8Mn_5 particles such as that in Figure 8(a), it can be concluded that the larger Al_8Mn_5 particles do not belong to the same population as the main lognormal distribution. The largest Al_8Mn_5 particles were very likely present in the shot chamber but there may also be other size populations associated with the different cooling rate and flow regimes in the different stages of HPDC: in the shot sleeve, the slow shot stage, the filling stage, and the intensification stage.

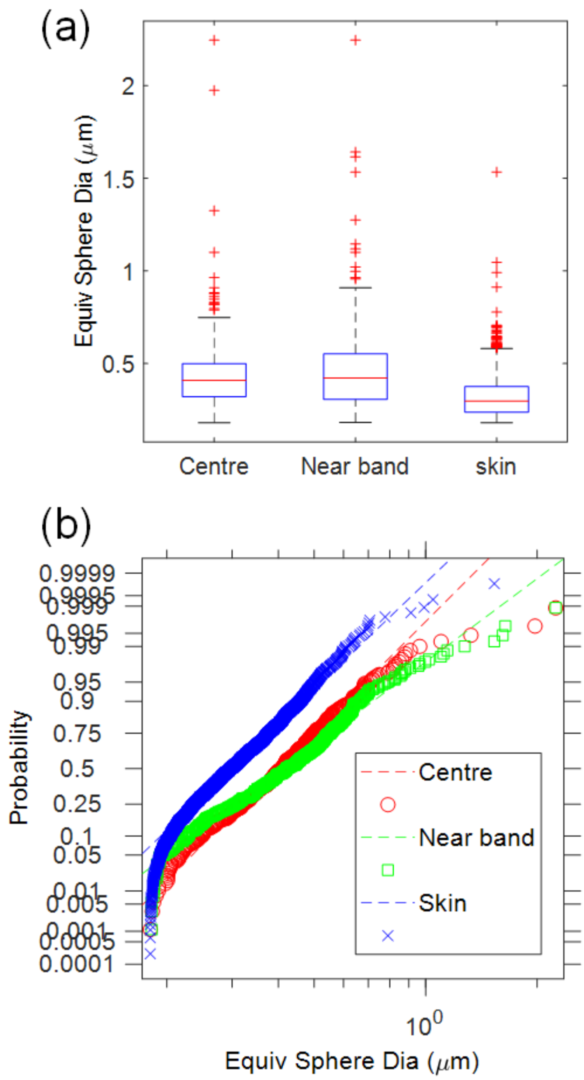

Figure 10: Analysis of the Al_8Mn_5 particle size data from FIB-tomography in Fig. 9 and Table 2. (a) Box plots showing the median, the 25th and 75th percentiles, and the outliers at large size. (b) lognormal probability plot to test for lognormality of the datasets at each location.

Considering now the distributions of Al_8Mn_5 particles in the three locations in the casting, it can be seen in Figures 9 and 10 and Table 2, that the Al_8Mn_5 size distributions were similar in the centre and defect band regions. For example, the size distributions from the centre and defect band overlap over most of the range from 1%-99% of the cumulative frequency plot in Figure 10(b), and the median Al_8Mn_5 size was similar (at 414 ±7 nm) (Table 2). Additionally, the tail at large size was similar in the centre and defect band, as can be seen in the volume occupied histograms in Figure 9(a), and the similar maximum Al_8Mn_5 particle size in the sampled volumes in Table 2. Thus, it is likely that the Al_8Mn_5 particle size distributions are similar throughout the interior regions of the castings.

In contrast, the Al_8Mn_5 size distribution was markedly different in the skin with significantly smaller and more numerous Al_8Mn_5 particles. For example, the Al_8Mn_5 distribution from the skin is shifted to smaller size (to the left) in Figure 10(b) and the median size is smaller by a factor of >4 in Table 2. There was also an order of magnitude higher number density (number per unit volume) of Al_8Mn_5 particles in the skin than in interior regions. This is shown in Table 2 and can be seen by eye in the rendered images in Figure 9(a). This higher number density is not simply due to the smaller Al_8Mn_5 size, but also because the volume fraction of Al_8Mn_5 particles was higher in the skin by a factor of 1.5-2 (Table 2).

Although a large number of Al-Mn particles were sampled by FIB tomography in this work (at least 449 in each region, Table 2), this technique is inherently limited by its small sampling volume. To partially offset this issue, within each type of region (the skin, band or centre), we selected each tomogram from different parts of the bar and sampled 3-6 tomograms (Table 2). For example, 4 tomograms were taken from randomly selected different parts of the skin, and all showed a higher volume fraction and smaller size of Al_8Mn_5 than the other two regions. Thus, the results in Figures 9 and 10 and Table 2 are likely to be generally valid across the whole bar. Figure 3 showed large variation in porosity distribution from sample to sample. From 2D backscatter electron imaging, there did not appear to be similarly large differences in the distributions of intermetallic compounds. However, further detailed FIB tomography work would be required to obtain quantitative detail on the variation in particle size distributions from sample to sample. Note that the most common porosity distribution in the HPDC bars was similar to Figure 3(b), and we performed our FIB slice and view characterisation and quantification on this type of sample.

3.6 Correlations between Al_8Mn_5 particles and $Mg_{17}Al_{12}$

In Figure 8(a), many bright Al_8Mn_5 particles appear close to eutectic regions on the 2D section. Therefore, the 3D FIB-tomography datasets were further explored to investigate any correlation between Al_8Mn_5 particles and eutectic $Mg_{17}Al_{12}$, noting from Figure 1 that Al_8Mn_5 forms before $Mg_{17}Al_{12}$.

In a previous FIB-tomography study on HPDC AZ91 [5], the eutectic $Mg_{17}Al_{12}$ was shown to form an interconnected scaffold-like network in 3D. The eutectic $Mg_{17}Al_{12}$ network was more profusely interconnected near the casting surface than at the casting centre which was attributed to the higher fraction of large ESCs near the centre resulting in a larger length scale of the $Mg_{17}Al_{12}$ network in the centre. A similar 3D $Mg_{17}Al_{12}$ microstructure was measured by FIB tomography in this work as shown in Figure 11. The $Mg_{17}Al_{12}$ (rendered in grey) forms a percolating network that is more intricately interconnected in the skin than in the defect band and centre.

In Figure 11 the Al_8Mn_5 particles are rendered with colour, where a different colour has been assigned to each distinct particle. It can be seen that some Al_8Mn_5 are in contact with $Mg_{17}Al_{12}$ and many are a significant distance away from $Mg_{17}Al_{12}$. Noting that the transparent phase is α-Mg, the numerous Al_8Mn_5 particles that are away from $Mg_{17}Al_{12}$ are fully surrounded by α-Mg in 3D. For those Al_8Mn_5 particles that share an interface with $Mg_{17}Al_{12}$, it is not possible with the techniques used to conclude whether $Mg_{17}Al_{12}$ nucleates on these pre-existing Al_8Mn_5 or whether Al_8Mn_5 particles are just pushed by the growth of α-Mg dendrites to the last liquid to solidify where they came into contact with $Mg_{17}Al_{12}$ during the final eutectic solidification. Further work is required to distinguish between these possibilities. A key finding from Figure 11 is that most Al_8Mn_5 particles do not contact $Mg_{17}Al_{12}$ in 3D.

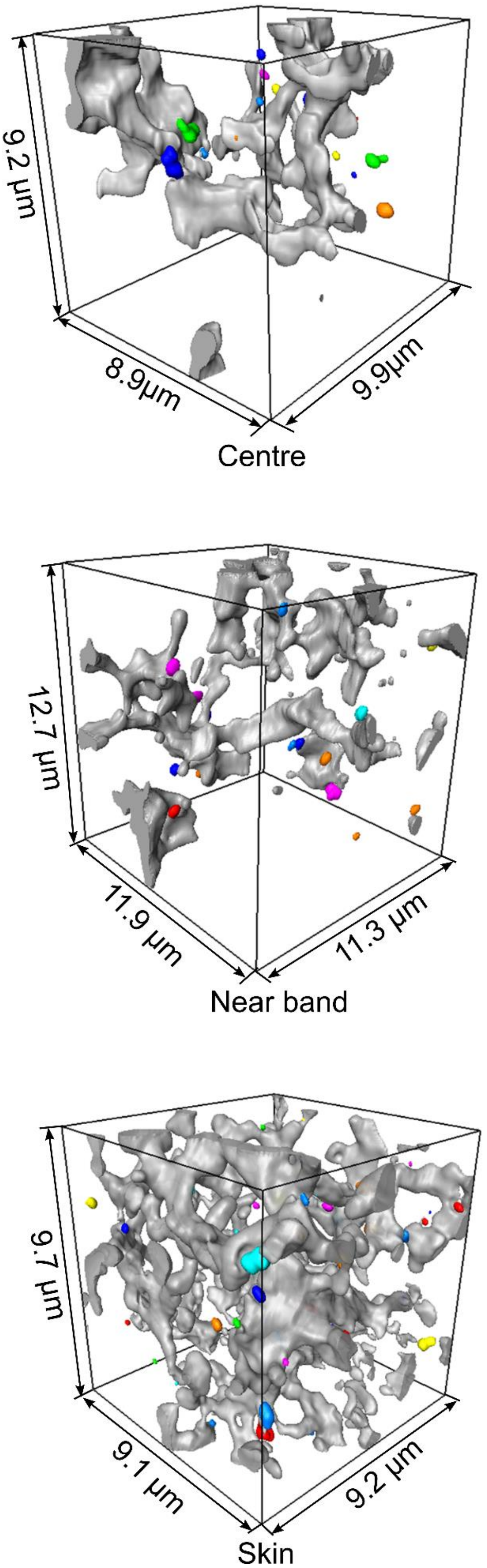

Figure 11. Rendered $Mg_{17}Al_{12}$ eutectic (grey) and Al_8Mn_5 (colours) from the FIB-tomography datasets in Figure. 9.

Comparing this HPDC study with past work at a controlled cooling rate of ~1 K s^{-1} [35], it can be concluded that the growth crystallography and twinning of larger Al_8Mn_5 particles in HPDC (Figure 6) is similar to slow cooled samples. However, the HPDC process generated a much wider variation in Al_8Mn_5 size distribution, number density, and morphology due to the wide range of cooling and flow conditions in the different stages of HPDC. This work has also identified significant differences in the Al_8Mn_5 size distribution in the skin and interior regions. The smaller particles, higher volume fraction and smaller interparticle spacing of Al_8Mn_5 particles in the skin region may partially contribute to the increased hardness reported in the skin [16]. In contrast, partial solidification in the shot sleeve ties up Mn in larger Al_8Mn_5 ESCs which will reduce the number density of Al_8Mn_5 particles and reduce the potential benefits that might be gained from smaller, more numerous particles.

4 Conclusions

Al-Mn intermetallic compounds have been characterised and quantified in high pressure die cast (HPDC) AZ91D test bars to understand the types of Al-Mn phases present, their faceted growth crystallography, and their size distribution in relation to the other phases and the key microstructural features in HPDC: the skin, the defect band, and $Mg_{17}Al_{12}$. The following conclusion can be drawn.

- Similar to Al_8Mn_5 particles in slow cooled (~1 K/s) AZ91D samples studied previously [35], Al_8Mn_5 particles in HPDC were often cyclic twins containing four orientations with $\{100\}_{BCR}$ twin planes. The facet morphology of large polyhedral Al_8Mn_5 particles could be described by combinations of {100}, {110}, and {112} facets.
- Al_8Mn_5 particles had a wide range of sizes and morphologies within the same HPDC component, but all could be broadly classified as equiaxed-polyhedral or complex-branched.
- The great majority of Al_8Mn_5 particles were sub-micrometre in size but there was a significant population of much larger (~5 μm) polyhedral particles whose size is similar to Al_8Mn_5 particles solidified at low cooling rate (1-3 K/s). These particles are concluded to be externally solidified crystals (ESCs) that nucleated and grew in the shot chamber analogous to the αMg ESCs.
- In all locations of the casting, the Al_8Mn_5 particle size distributions were reasonably well-described by lognormal distributions, accounting for the presence of an additional population(s) of larger grains associated with Al_8Mn_5 ESCs from the shot chamber.
- There were significant differences in the Al_8Mn_5 particle size and number density in the centre compared with the HPDC skin. The skin region had a median Al_8Mn_5 particle size (equivalent sphere diameter) of 99 nm, whereas the centre had a median Al_8Mn_5 size of 408 nm. The skin contained an order of magnitude higher number of Al_8Mn_5 particles per unit volume than interior regions
- 3D imaging showed that some Al_8Mn_5 particles were in contact with eutectic $Mg_{17}Al_{12}$ but the majority of Al_8Mn_5 particles were surrounded by α-Mg.
- This study has shown that HPDC of AZ91D generates numerous Al_8Mn_5 particles with diameter 100-400nm and a small interparticle spacing. Partial solidification in the

shot sleeve ties up Mn in larger Al_8Mn_5 ESCs which reduces the number density of Al_8Mn_5 particles.

Acknowledgements

Financial support from EPSRC (UK) under grant number EP/N007638/1 (the Future LiME Hub) is gratefully acknowledged. This work was partly supported by the National Natural Science Foundation of China (51904352). The authors acknowledge use of characterisation facilities within the Harvey Flower Electron Microscopy Suite, Department of Materials, Imperial College London.

References:

1 X. Li, S.M. Xiong, and Z. Guo: *J. Mater. Process. Technol.*, 2016, vol. 231, pp. 1–7.

2 A. Luo and A. Sachdev: *Int. J. Met.*, 2010, vol. 4, pp. 51–9.

3 A. Bowles, K. Nogita, M. Dargusch, C. Davidson, and J. Griffiths: *Mater. Trans.*, 2005, vol. 45, pp. 3114–9.

4 S. Biswas, F. Sket, M. Chiumenti, I. Gutiérrez-Urrutia, J.M. Molina-Aldareguía, and M.T. Pérez-Prado: *Metall. Mater. Trans. A Phys. Metall. Mater. Sci.*, 2013, vol. 44, pp. 4391–403.

5 A. V. Nagasekhar, C.H. Cáceres, and C. Kong: *Mater. Charact.*, 2010, vol. 61, pp. 1035–42.

6 B. Zhang, A. V. Nagasekhar, T. Sivarupan, and C.H. Caceres: *Adv. Eng. Mater.*, 2013, vol. 15, pp. 1059–67.

7 P. Sharifi, J. Jamali, K. Sadayappan, and J.T. Wood: *J. Mater. Sci. Technol.*, 2018, vol. 34, pp. 324–34.

8 K.V. Yang, M.A. Easton, and C.H. Cáceres: *Mater. Sci. Eng. A*, 2013, vol. 580, pp. 191–5.

9 S. Barbagallo, H.I. Laukli, O. Lohne, and E. Cerri: *J. Alloys Compd.*, 2004, vol. 378, pp. 226–32.

10 D.G.L. Prakash and D. Regener: *J. Alloys Compd.*, 2008, vol. 461, pp. 139–46.

11 C.M. Gourlay and A.K. Dahle: *Nature*, DOI:10.1038/nature05426.

12 P. Sharifi, J. Jamali, K. Sadayappan, and J.T. Wood: *Metall. Mater. Trans. A*, DOI:10.1007/s11661-018-4633-0.

13 H. Cao and M. Wessén: *Int. J. Cast Met. Res.*, 2005, 18, vol. 18.

14 X. Li, S.M. Xiong, and Z. Guo: *Mater. Sci. Eng. A*, 2015, vol. 633, pp. 35–41.

15 C.M. Gourlay, H.I. Laukli, and A.K. Dahle: *Metall. Mater. Trans. A*, 2007, vol. 38, pp. 1833–44.

16 C.H. Cáceres, J.R. Griffiths, A.R. Pakdel, and C.J. Davidson: *Mater. Sci. Eng. A*, 2005, vol. 402, pp. 258–68.

17 E. Deda, T.D. Berman, and J.E. Allison: *Metall. Mater. Trans. A*, 2017, vol. 48, pp. 1999–2014.

18 L.-Y. Wei, H. Westengen, T.K. Aune, and D. Albright: *Magnes. Technol. 2000*, 2013, pp. 153–60.

19 R.M. Wang, A. Eliezer, and E. Gutman: *Mater. Sci. Eng. A*, 2003, vol. 344, pp. 279–87.

20 G. Zeng, X. Zhu, S. Ji, and C.M. Gourlay: *Magnesium Technology 2018*, pp.137-144. Springer, Cham, 2018

21 V.Y. Gertsman, J. Li, S. Xu, J.P. Thomson, and M. Sahoo: *Metall. Mater. Trans. A Phys. Metall. Mater. Sci.*, 2005, vol. 36, pp. 1989–97.

22 O. Lunder, K. Nişanciogu, and R.S. Hansen: *SAE Tech. Pap.*, 1993, pp. 117–26.

23 M. Liu and G.-L. Song: *Corros. Sci.*, 2013, vol. 77, pp. 143–50.

24 M. Lugo, M.A. Tschopp, J.B. Jordon, and M.F. Horstemeyer: *Scr. Mater.*, 2011, vol. 64, pp. 912–5.

25 Y. Uematsu, K. Tokaji, and M. Matsumoto: *Mater. Sci. Eng. A*, 2009, vol. 517, pp. 138–45.

26 ASTM B94: *Annu. B. ASTM Stand.*, 2018, pp. 1–6.

27 Thermo-Calc software: 2019.

28 G. Zeng, K. Nogita, S. Belyakov, J.W. Xian, S.D. McDonald, K. V. Yang, H. Yasuda, and C.M. Gourlay. *Magnesium Technology 2017*, pp. 597-603. Springer, Cham, 2017.

29 L. Peng, G. Zeng, T.C. Su, H. Yasuda, K. Nogita, and C.M. Gourlay: *Jom*, 2019, vol. 71, pp. 2235–44.

30 C.P. Corby, N.J. Ricketts, M. Qian, and R.D. Bailey: *Magnes. Technol. 2004*, 2004, pp. 209–14.

31 C. Bi, S. Xiong, X. Li, and Z. Guo: *Metall. Mater. Trans. B*, 2016, vol. 47, pp. 939–47.

32 L. Wang, T. Nguyen, G. Savage, and C. Davidson: in *International Journal of Cast Metals Research*, vol. 16, 2003, pp. 409–17.

33 H.I. Laukli, A. Graciotti, O. Lohne, H. Gjestland, and S. Sannes: in *NADCA Transactions*, 2002, pp. T02-035, pp.1–4.

34 J. Song, S.M. Xiong, M. Li, and J. Allison: *J. Alloys Compd.*, 2009, vol. 477, pp. 863–9.

35 G. Zeng, J.W. Xian, and C.M. Gourlay: *Acta Mater.*, 2018, vol. 153, pp. 364–76.

36 F. Bachmann, R. Hielscher, and H. Schaeben: *Solid State Phenom.*, 2010, vol. 160, pp. 63–8.

37 Z. Fan, G. Liu, and Y. Wang: *J. Mater. Sci.*, 2006, vol. 41, pp. 3631–44.

38 Y. Du, J. Wang, J. Zhao, J.C. Schuster, F. Weitzer, R. Schmid-Fetzer, M. Ohno, H. Xu, Z.K. Liu, S. Shang, and W. Zhang: *Int. J. Mater. Res.*, 2007, vol. 98, pp. 855–71.

39 R. Sarvesha, W. Alam, A. Gokhale, T.S. Guruprasad, S. Bhagavath, S. Karagadde, J. Jain, and S.S. Singh: *Mater. Sci. Eng. A*, 2019, vol. 759, pp. 368–79.

40 M. Ellner: *Metall. Trans. A*, 1990, vol. 21, pp. 1669–72.

41 S. Thimmaiah, Z. Tener, T.N. Lamichhane, P.C. Canfield, and G.J. Miller: *Zeitschrift fur Krist. - Cryst. Mater.*, 2017, vol. 232, pp. 601–10.

42 S. Balanetskyy, D. Pavlyuchkov, T. Velikanova, and B. Grushko: *J. Alloys Compd.*, 2015, vol. 619, pp. 211–20.

43 S. Yao, S. Liu, G. Zeng, X. Li, T. Lei, Y. Li, and Y. Du: *Metals (Basel).*, 2019, vol. 9, p. 460.

44 K. Yoshida, T. Yamamoto, and S. Nagata: *Jpn. J. Appl. Phys.*, 1974, vol. 13, pp. 400–10.

45 S. Lun Sin, D. Dubé, and R. Tremblay: *Mater. Charact.*, 2007, vol. 58, pp. 989–96.

46 M.Y. Wang, J.J. Williams, L. Jiang, F. De Carlo, T. Jing, and N. Chawla: *Metallogr. Microstruct. Anal.*, 2012, vol. 1, pp. 7–13.

47 T. Kubo, Y. Wakashima, H. Imahashi, and M. Nagai: *J. Nucl. Mater.*, 1986, vol. 138, pp. 256–67.

48 G. Timelli and F. Bonollo: *Mater. Sci. Eng. A*, 2010, vol. 528, pp. 273–82.

49 B.G. Dietrich, H. Becker, M. Smolka, A. Keßler, A. Leineweber, and G. Wolf: *Adv. Eng. Mater.*, 2017, vol. 19, p. 1700161.

Al_8Mn_5 in high pressure die cast AZ91: twinning, morphology and size distributions

G. Zeng[1,2,*], S.S. Shuai[3], X. Zhu[4], S. Ji[4], J.W.Xian[2] and C. M. Gourlay[2*].

[1]School of Materials Science and Engineering, Central South University, Changsha 410083, China
[2]Department of Materials, Imperial College London, London, SW7 2AZ, UK
[3]State Key Laboratory of Advanced Special Steel, School of Materials Science & Engineering, Shanghai University, 200444, Shanghai, China
[4] BCAST, Institute of Materials & Manufacturing, Brunel University London, Uxbridge, UB8 3PH, UK

* corresponding authors: g.zeng@csu.edu.cn and c.gourlay@imperial.ac.uk

Abstract

Manganese-bearing intermetallic compounds (IMCs) are important for limiting micro-galvanic corrosion of magnesium-aluminium alloys and can initiate cracks under tensile load. Here we use electron backscatter diffraction (EBSD), deep etching, and focussed ion beam (FIB) tomography to investigate the types of Al-Mn phases present, their faceted growth crystallography, and their three-dimensional distribution at different locations in high pressure die cast (HPDC) AZ91D. The Al-Mn particle size distributions were well-described by lognormal distributions but with an additional population of externally solidified crystals (ESCs) formed in the shot chamber analogous to α-Mg ESCs. The large Al_8Mn_5 particles were cyclic twinned. Differences in the particle size distributions and number density in the centre compared with the HPDC skin are identified, and the spatial relationship between $Mg_{17}Al_{12}$ and Al-Mn particles is explored.

Keywords AZ91, high pressure die casting, intermetallics

Introduction

Automotive magnesium components are often Mg-Al-based alloys produced by high pressure die casting (HPDC). When conducted with an optimised die, process parameters and vacuum system [1,2], HPDC can mass produce large, thin-walled, complex shapes containing microstructures with fine α-Mg grains (5-20 μm) [3,4], and a fine-scaled percolating eutectic $Mg_{17}Al_{12}$ network [5,6]. While a large body of research has investigated microstructure formation in Mg HPDC, including the formation of α-Mg grains [3,4,7], the surface 'skin' [4,8], the eutectic $Mg_{17}Al_{12}$ [5,9,10], and casting defects [11–17], less work has explored the formation of Al-Mn-(Fe) intermetallic particles [18–21]. These particles play an important role in determining micro-galvanic corrosion in HPDC Mg parts [22,23] and can initiate cracks under tensile loading [24,25].

Most Mg-Al-based HPDC alloys (e.g. AM50A, AM60B, AZ91D [26]) contain sufficient Mn and Al that Al_8Mn_5 begins to form before α-Mg during solidification. For example, Figure 1 shows the sequence of phase formation assuming Scheil solidification of AZ91D with the composition in Table 1, calculated with the Thermo-Calc TCMG magnesium database version 4 [27]. It can be seen that Al_8Mn_5 is the first solid phase to form, and becomes stable ~44K above the α-Mg liquidus temperature for this composition. It has been confirmed by in-situ X-ray imaging that Al_8Mn_5 forms at higher temperature (i.e. earlier on cooling) than α-Mg in a similar alloy [28,29]. A consequence of this in HPDC is that Al_8Mn_5 can form and settle in the holding pot [29,30], for example during temperature drops when charging the furnace with new ingots, leading to die casting sludge [30]. Furthermore, in cold chamber HPDC, heat loss in the shot chamber can cause Al_8Mn_5 formation prior to injection as Al_8Mn_5 externally solidified crystals (ESCs) [20] in addition to the α-Mg ESCs that are widespread in HPDC Mg components [3,14,31]. This occurs because a feature of Mg HPDC is partial solidification in the shot chamber that leads to large α-Mg externally solidified crystals (ESCs) being injected into the cavity [3,32]. The volume fraction of α-Mg ESCs has been shown to depend on the melt superheat, the fill fraction and the temperature of the sleeve walls and plunger tip, and is typically 10-30 vol.% [3,14,31,33]; similar factors might be expected to determine the formation of Al_8Mn_5 ESCs.

Table 1. Composition of the AZ91D alloy used (weight percent).

Mg	Al	Zn	Mn	Fe	Ni	Cu	Si	Be
bal.	8.95	0.72	0.19	<0.001	<0.001	0.001	0.039	0.0007

Figure 1 shows that Al_8Mn_5 continues forming along with α-Mg below the α-Mg liquidus temperature until ~ 510°C when other Al-Mn IMCs start forming ($Al_{11}Mn_4$ and then Al_4Mn). Therefore, in HPDC, Al-Mn IMCs are expected to form in all stages of the process: in the shot chamber, during filling and during the intensification stage. According to calculations linked with Figure 1, at the end of Scheil solidification, the total mass fraction of Al-Mn IMCs (Al_8Mn_5, $Al_{11}Mn_4$ and Al_4Mn) is 0.25% of which 95% is Al_8Mn_5 for the composition in Table 1.

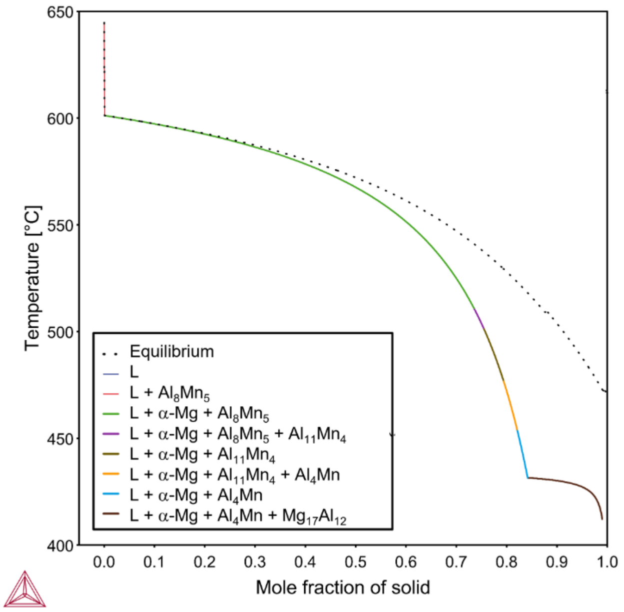

Figure 1: Phase formation during Scheil solidification up to 99% solid for Mg-8.95Al-0.72Zn-0.19Mn (wt%). Calculated with Thermo-Calc TCMG magnesium database version 4 [27].

Past work on Al-Mn particles in HPDC AZ91D has generally used TEM [18,19,21]. That work has deduced that most Al-Mn particles in HPDC AZ91D are 100 nm to 1μm in size. The main phase present has been found to be Al_8Mn_5 and another phase with higher Al content (possibly $Al_{11}Mn_4$) has also been reported [18]. While these TEM studies enable high resolution imaging, they did not explore the statistical variation in Al-Mn particle size and shape versus position in the cross-section. This is an important question in HPDC parts since they usually have highly non-uniform microstructures. They typically have a surface layer (a skin) of distinctly different microstructure that is usually free of porosity and harder than more central regions, one or more bands of porosity, various forms of macrosegregation, and ESCs that tend to be concentrated towards the centre of cross-sections (e.g. [15,16,33,34]).

In this paper, we investigate the types of Al-Mn phases present, their faceted growth crystallography, and their three-dimensional distribution at different locations in high pressure die cast AZ91D. The specific aims are: (i) to compare the Al_8Mn_5 growth crystallography and twinning formed in HPDC with past work at sand casting cooling rates [35]; (ii) to quantify the 3D size, morphology and spatial distribution of Al-Mn particles in different locations in HPDC AZ91D: the skin, the defect band, and the centre; and (iii) to explore any correlations between Al-Mn particles and eutectic $Mg_{17}Al_{12}$ in 3D.

Methods

~6 kg of AZ91D Mg alloy with composition in Table 1 was melted in a mild steel crucible and held at 675°C (~ 75°C superheat) under a cover gas of ~3 vol% SF_6 in N_2. HPDC was conducted using a Frech DAK 450-54 cold chamber HPDC machine and the multi-cavity die that produces the casting in Figure 2. The die was preheated to 150°C, a portion of the melt was ladled into the shot chamber to a fill fraction of ~0.5, and the following set parameters were used: slow shot phase of 0.3 $m.s^{-1}$, fast shot phase of 4 $m.s^{-1}$, and intensification pressure of 36 MPa. The casting analysed in this work was made after six pre-shots.

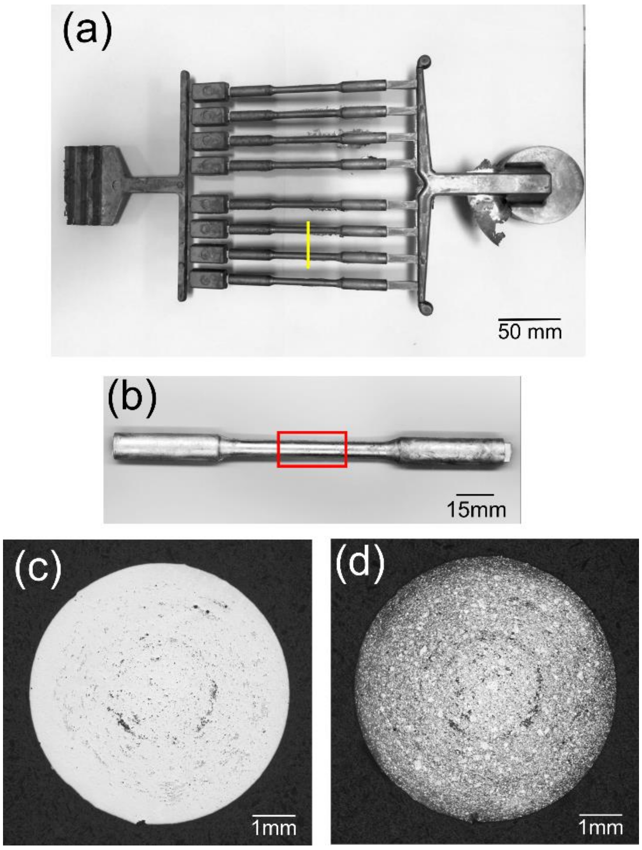

Figure 2 (a-b) Photographs of the HPDC part. The sectioning plane is indicated by superimposed lines. (c) as-polished optical micrograph.(d) the same section after etching.

Samples for microstructural analysis were cut from the centre of the gauge length into slices of 10mm x 10mm x 0.5mm. Metallographic polishing was carried out down to 0.05μm colloidal silica by standard preparation methods. Some samples were etched in a solution of 200ml ethylene glycol, 68ml distilled water, 4ml nitric acid and 80 ml acetic acid. Both etched and polished samples were analysed in a Zeiss AURIGA field emission gun SEM (FEG-SEM) with an Oxford Instruments INCA x-sight energy dispersive X-ray spectroscopy (EDX) detector and a BRUKER e-Flash^{HR} electron backscatter diffraction (EBSD) detector. For EBSD characterisation, the final step of preparation was Ar-ion milling for 40 min in a Gatan PECSII instrument. The 4 kV-accelerated beam hit the sample rotating at 2 rpm, at a grazing incidence angle of 4°. Electron beam accelerating voltage of 20kV, working distance of 15mm, aperture size of 120mm, and beam current 80µA were used for EBSD measurements. Bruker ESPRIT 2.1 software was used to index the obtained EBSD patterns. EBSD datasets were analysed using MATLAB™ 9.2 (Mathworks, USA) with the MTEX 5.1 toolbox [36]. Accelerating voltage of 10kV, working distance of 5mm, aperture size of 60mm, and beam current 80µA were used for EDS analysis. EDS spectrum was calibrated with a Si standard sample prior to each electron microscopy session.

To investigate the 3-dimensional (3D) morphology of the Al-Mn intermetallics directly, α-Mg was selectively etched using a solution of 4% nitric acid in ethanol. To quantify the 3D size distribution of Al-Mn intermetallics, focussed ion beam (FIB) tomography was conducted in a Zeiss AURIGA FG-SEM at 30 kV with 52° tilt angle. The slice distance was 90 nm and the milling current was 200pA. Serial-sectioning secondary electron images were used. For FIB tomography, 2D slices were aligned, cropped, and processed by an anisotropic diffusion filter in ImageJ (US NIH, USA). 3D reconstruction and crystallographic analysis was performed using Avizo 9.2 (Visualization Science Group, France) and MATLAB 9.2™. The voxel size for FIB tomography was bounded by the slice spacing of 90nm. Al_8Mn_5 particles with equivalent diameter ≧ 180nm were quantified.

To study porosity bands in 3D, X-ray micro-tomography was carried out on a North Star Imaging (NSI) Micro-CT. The system is equipped with a 225 kV X-ray source with a minimum focal spot size of 2 µm and a Perkin Elmer flat panel detector (2048×2048 pixels at 16bit depth). During a CT scan, the sample was illuminated by cone beam X-rays which were transmitted through the 360° rotating specimen and then illuminated on the flat panel detector. The X-ray beam was filtered using a 0.25 mm Cu filter to reduce beam-hardening effects, and an acceleration voltage of 80kV and target current of 35µA was selected to optimise image quality. 1440 two-dimensional projections were captured over 360° with an exposure time of 1000ms. 3D reconstruction was performed in Avizo 9.2 and resulted in a 3D spatial resolution with voxel size of 2.2 µm x 2.2 µm x 2.2 µm.

3 Results and Discussion

3.1 General microstructural features

At the centre of the gauge length, the AZ91D samples contained the typical microstructural features and defects of HPDC reported in past work (e.g. [3,7,12,14,16,33,34,37]). For example, annular rings of porosity can be seen in the as-polished condition in Figure 2(c), a dark band of macrosegregation can be seen in the same location as the main porosity band in Figure 2(d) after light etching, and a high fraction (~30 vol%) of α-Mg ESCs can be seen throughout much of the cross-section in Figure 2(d). However, the detail of these features differed significantly from casting to casting and between bars in the same casting as shown in the X-ray tomographs in Figure 3. The left-hand images are reconstructed volumes near the centre of the gauge length showing the 3D distribution of porosity. The right-hand images are viewed along the tensile rod axis to highlight the radial distribution of porosity. There are major differences in the porosity in the two samples. The sample in Figure 3(b) has a localised annular ring of porosity and a high fraction of porosity within this ring. The sample in Figure 3(a) has more diffuse porosity and a less-well defined porosity ring but has the same trend of a higher fraction of porosity within the annular porosity band. Despite the differences, in both samples, the main annular ring of porosity is at a similar radial position. The projection images along the rod axes also reveal the surface 'skin' as an outer ring of essentially zero porosity. This is particularly clear in Figure 3(a) where the abrupt change in porosity demarcates the edge of the skin.

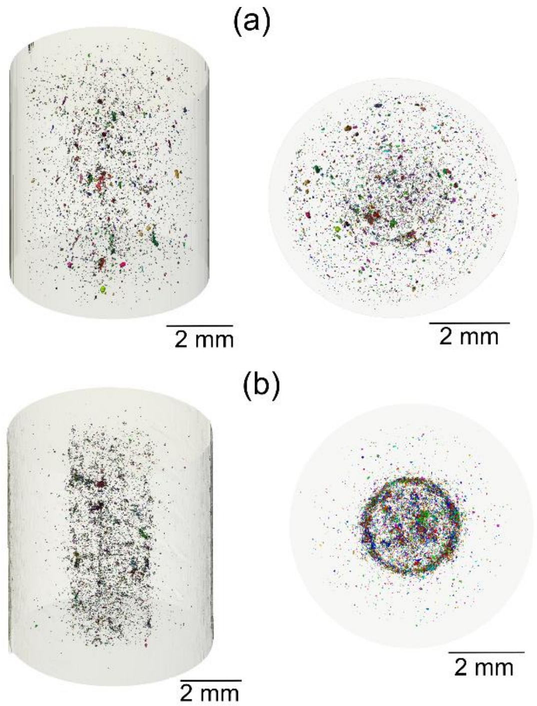

Figure 3 (a-b) X-ray tomograms of porosity near the centre of the gauge-length of typical castings. Porosity is rendered as solid, material (Mg, $Mg_{17}Al_{12}$ and Al-Mn IMCs) is plotted as semi-transparent. Left-hand side: perspective view. Right-hand side: projection view along the tensile rod axis.

The typical α-Mg microstructure is shown in more detail in Figure 4(a)-(b). The micrograph in Figure 4(a) shows the complex mixture of dendritic α-Mg ESCs, ESC fragments and in-cavity solidified grains. Figure 4(b) is an EBSD orientation map (IPF-y) of the α-Mg phase from a similar region where the grains have been coloured by their mean-orientation. The grains form a complex multimodal microstructure with, in this case, two large ESCs surrounded by smaller α-Mg grains that are probably a mixture of α-Mg ESC fragments and in-cavity solidified grains.

The typical features of intermetallic compounds in the HPDC bars are overviewed in Figure 4(c) and (d). It can be seen that the eutectic $Mg_{17}Al_{12}$ phase appears as isolated regions in 2D sections (Figure 4(c)) but actually forms a percolating $Mg_{17}Al_{12}$ network in 3D as revealed by imaging after selective dissolution of the α-Mg in Figure 4(d). Figure 4(c) and (d) also contains bright particles that are Al-Mn compounds. In the 2D section these appear both within the α-Mg grains and near the $Mg_{17}Al_{12}$ phase (Figure 4(c)). After deep etching, it can be seen that many Al-Mn particles are attached to the $Mg_{17}Al_{12}$ network (Figure 4 (d)).

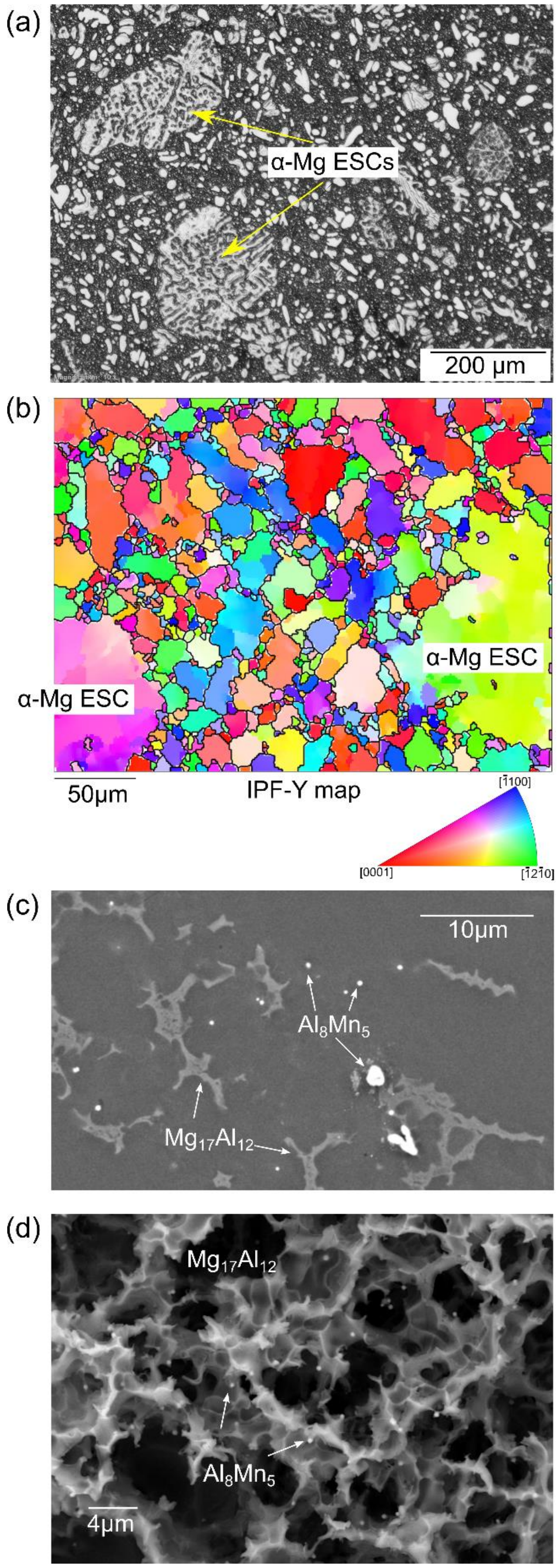

Figure 4: Typical microstructural features in the HPDC AZ91 samples. (a) mixture of α-Mg ESCs and in-cavity solidified grains. (b) EBSD orientation map (IPF-Y) of the α-Mg phase. (c) 2D section of $Mg_{17}Al_{12}$ and Al_8Mn_5 phases. (d) 3D microstructure of $Mg_{17}Al_{12}$ network and attached Al_8Mn_5 particles, revealed after selective etching of α-Mg .

The remainder of this paper focuses on the Al-Mn intermetallic compounds and their relationship to the microstructural features summarised in this section.

3.2 Twinned Al_8Mn_5 in HPDC AZ91D

Al-Mn intermetallics were identified by combining EDS with EBSD. A typical EDS point analysis from an Al-Mn particle is shown in Figure 5(a). The particle contains 59at%Al - 40at%Mn and there are also small Mg, Si and Fe peaks, each present at less than 1 at%. Since the solubility of Mg in Al-Mn intermetallics is negligible [38], the small Mg peak is likely to be α-Mg in the interaction volume. The small Si peak is probably Si dissolved in the particle, consistent with past work that has detected a small Si content in Al-Mn IMCs [18,39]. The low Fe content in the particle is due to the high-purity AZ91D used in this study (with <10ppm Fe, Table 1).

An EBSD pattern from the Al-Mn particle is shown in Figure 5(b). This could be readily distinguished as the rhombohedral Al_8Mn_5 phase [40,41] using the Hough transform-based method in Bruker ESPRIT 2.1, and is indexed in Figure 5(c) in the hexagonal setting R3mH. Although various Al-Mn intermetallics are known to exist and three are expected to form (Al_8Mn_5, $Al_{11}Mn_4$ and Al_4Mn) according to Scheil calculations using current thermodynamic databases [27], the strong crystallographic differences between these phases enabled Al_8Mn_5 to be clearly distinguished. Al_8Mn_5 is also consistent with the EDS measurement of 59at%Al - 40at%Mn. Note that rhombohedral Al_8Mn_5 is also known as γ_2 [42] and LT-AL_8Mn_5 [43] , and is a gamma brass with Strukturbericht designation $D8_{10}$. It is useful to index this crystal structure in the non-standard body-centred rhombohedral (BCR) setting as discussed in refs. [35,41,44].

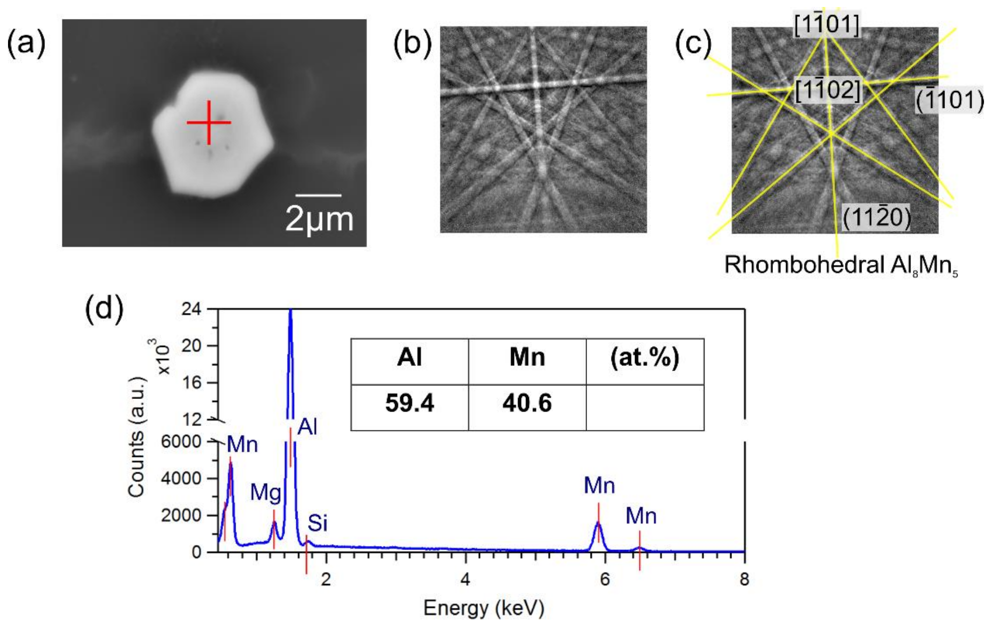

Figure 5: (a) EDS spectrum from the particle in (b). (c) EBSD pattern from the same particle. (d) EBSD pattern indexed as rhombohedral Al_8Mn_5 ($D8_{10}$).

Rhombohedral Al_8Mn_5 was the only Al-Mn intermetallic detected in the HPDC AZ91D samples by SEM-based techniques in this work. This is reasonably consistent with Scheil calculations within Thermo-Calc Software TCMG magnesium database version 4 [27] which show that ~95% of all the Al-Mn phases formed during Scheil solidification are Al_8Mn_5 (using the composition in Table 1). If $Al_{11}Mn_4$ and/or Al_4Mn were present in the HPDC samples, they were either too low in volume fraction or too small to be detected. The B2-Al(Mn,Fe) phase identified in AZ91 in ref. [35] was not detected in this work, most likely because the AZ91 used here (Table 1) had a very low Fe content (<10 ppm).

It was found that most HPDC Al_8Mn_5 particles were cyclic twinned containing up to four orientations, similar to the Al_8Mn_5 particles at low cooling rate identified in ref. [35]. For example, Figure 6(a) is a typical ~5 μm HPDC Al_8Mn_5 particle and Figure 6(b) is its EBSD orientation map showing the presence of three orientations within the particle. Note that the grey pixels have unknown orientation due to low EBSD pattern quality in this region. The three orientations are plotted in pole figures in Figure 6(c) which show that all three orientations share three common $\{100\}_{BCR}$ planes and each orientation shares a common $\{110\}_{BCR}$ plane with one of the other orientations. This orientation relationship between the three Al_8Mn_5 orientations is shown geometrically in Figure 6(e) which is a plot of the BCR unit cell wireframes using the EBSD-measured Euler angles and coloured consistent with Figure 6(b)-(c). The green orientation was not measured experimentally for this 2D section of the particle but is likely to be present in the 3D particle based on the findings in our previous work [35]. Note that the BCR unit cell of Al_8Mn_5 has rhombohedral angle ~89° [40,41] and so appears as near-cubes in Figure 6(e). Figure 6(f) is a digital section through the geometrical model in Figure 6(e). It can be seen that the Al_8Mn_5-Al_8Mn_5 interfaces in the sliced BCR model have similar angular arrangement with the experimental interfaces in Figure 6(b), consistent with the interfaces being $\{100\}_{BCR}$. The cyclic growth twinning of Al_8Mn_5 with $\{100\}_{BCR}$ twin planes can be understood by noting that, with a rhombohedral angle of ~89° [40,41], the crystal is pseudo-cubic which gives the possibility for growth twins with $\{100\}_{BCR}$ interfaces by ~90° rotations around the three $<100>_{BCR}$ axes [35].

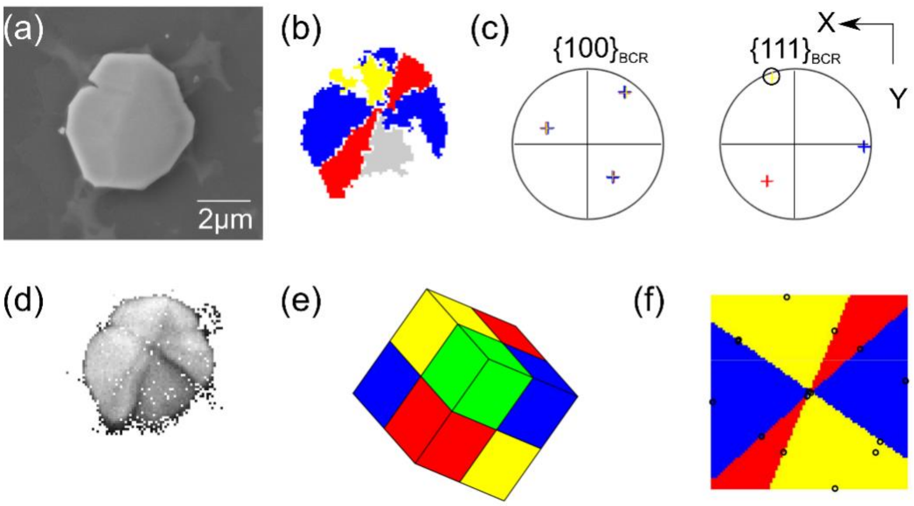

Figure 6. Cyclic growth twinning of Al_8Mn_5 particles in HPDC AZ91. (a) SEM image, (b) EBSD orientation map in RGBY colour scheme,(Grey region has unknown orientation due to low pattern quality). (c) $\{100\}_{BCR}$ and $\{111\}_{BCR}$ pole figures showing the three orientations. (d) band contrast map showing grain boundaries. The three BCR unit cell orientations (plus a green orientation that was not present in the cross-section). (f) $\{100\}_{BCR}$ twin planes revealed by sectioning the BCR geometrical model.

In the HPDC AZ91D sample studied here, it was found that all equiaxed polyhedral Al_8Mn_5 particles that were large enough for EBSD mapping were cyclic twinned. Comparing Figure 6 in this paper with the TEM images in Fig. 4(a) in ref [19] and Fig. 7(b) in ref. [21], it is likely that the HPDC Al_8Mn_5 particles in references [19,21] contain sector-twins and were also cyclic twinned, although those authors did not study or mention this.

Having confirmed that the majority of Al-Mn particles are Al_8Mn_5 by combined EDS and EBSD, Al_8Mn_5 could be distinguished in backscattered electron (BSE) images due to the much higher atomic-number of Mn compared with Mg and Al. For example, in Figure 2(c), the numerous bright particles are Al_8Mn_5 and the lighter grey particles are $Mg_{17}Al_{12}$.

3.3 Al_8Mn_5 morphologies

The HPDC AZ91D bars contained a range of Al_8Mn_5 morphologies that could be broadly classified into two categories: equiaxed-polyhedral and complex-branched particles. A representative selection is shown in Figure 7 where Figure 7(a) are equiaxed-polyhedral morphologies, and Figure 7(b) are a range of complex-branched morphologies. Each column represents a different location in the test bars: the centre of the cross-section, the defect band, and the skin. It can be seen that similar morphologies were present at each location of the castings, although the size distributions were different as will be discussed in detail later in this paper.

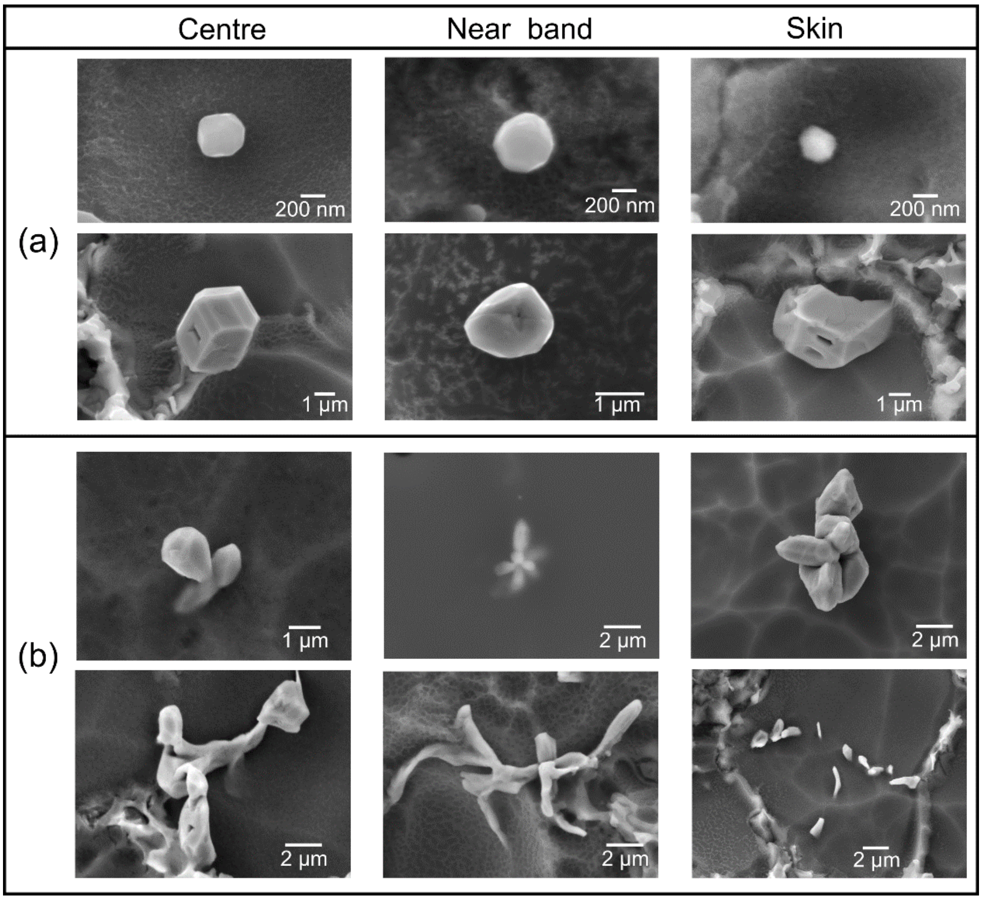

Figure 7: Typical range of Al_8Mn_5 morphologies in one HPDC AZ91 sample. SE-SEM images after selective etching of the α-Mg. (a) equiaxed polyhedral particles, (b) complex branched particles.

It has been shown by in-situ X-ray imaging of AZ91 solidification at low cooling rate [28,29], that the Al_8Mn_5 particles that form in the early stages of solidification are equiaxed polyhedral and it is likely, therefore, that the equiaxed-polyhedral particles in these HPDC samples also formed in the earlier stages of solidification. The complex-branched particles in the bottom row of Figure 7(b) may have formed relatively late during a eutectic-type reaction when the remaining liquid regions were tortuous channels. This is consistent with Figure 1 which shows that, for Scheil solidification, Al_8Mn_5 forms both as a primary phase prior to α-Mg formation (the red line) and also by a eutectic-type reaction with α-Mg (the green line), $L \rightarrow \alpha\text{-Mg} + Al_8Mn_5$, over a range of temperature up to ~70% solid. However, further work is required to confirm that the complex-branched particles in the bottom row of Figure 7(b) formed in this eutectic-type reaction.

Past work on investment cast AZ91 reported dendritic Al_8Mn_5 near the surface [45]. In the HPDC samples studied here, the complex-branched particles occasionally had dendritic morphology (e.g. some in the top row of Figure 7(b)) but these were present at all locations in the casting. FIB serial sectioning on one branched-faceted Al_8Mn_5 crystal with morphology similar to the top row of Figure 7(b) was conducted to explore its formation. The FIB slices confirmed that, in this case, the branched structure grew from a common centre. At the same time, it is also possible that other complex-branched Al_8Mn_5 similar to the top row of Figure 7(b) are clusters of equiaxed-polyhedral particles that were swept together during solidification.

3.4 Al_8Mn_5 externally solidified crystals (ESCs)

The Al_8Mn_5 particles had a wide range of sizes spanning from <100 nm to >5μm, which is significantly broader than in previous work at sand-casting cooling rates. For example, in ref. [35], the Al_8Mn_5 particle size varied from 4-14 μm for a cooling rate of ~1 $K.s^{-1}$. Figure 8(a) is a typical micrograph of a region containing Al_8Mn_5 particles with a wide size range in the HPDC samples. A ~4μm Al_8Mn_5 particle can be seen that is an order of magnitude larger than the numerous smaller Al_8Mn_5 particles in the surrounding material. It is likely that the large particle is an Al_8Mn_5 ESC that nucleated and grew in the shot chamber at low cooling rate before being injected into the die cavity analogous to the α-Mg ESCs in Figure 2(d) and 4(a)-(b), whereas the smaller Al_8Mn_5 nucleated and grew at higher cooling rate. This can be concluded based on three factors: (i) the larger (~5 μm) Al_8Mn_5 particles in (e.g. Figures 5(a), 6(a) and 8(a)) are within the range of Al_8Mn_5 particle sizes reported for a cooling rate of ~1 K.s^{-1} in past work [35], indicating that they did not form in the die cavity at high cooling rate; (ii) as will be shown in the next section, the larger (~5 μm) Al_8Mn_5 particles do not belong to the same population as the smaller Al_8Mn_5 particles and the Al_8Mn_5 exhibit a multi-model grain size distribution similar to α-Mg grains in HPDC parts containing α-Mg ESCs (e.g. [3]); and (iii) Al_8Mn_5 ESCs are expected since these samples contain α-Mg ESCs (Figure 4) and Al_8Mn_5 is stable above the α-Mg liquidus (Figure 1) for the composition in Table 1 [27]. Note that abnormally large Al_8Mn_5 particles in HPDC parts can be even larger, with a 20μm Al_8Mn_5 particle found in HPDC AM50 in ref. [20].

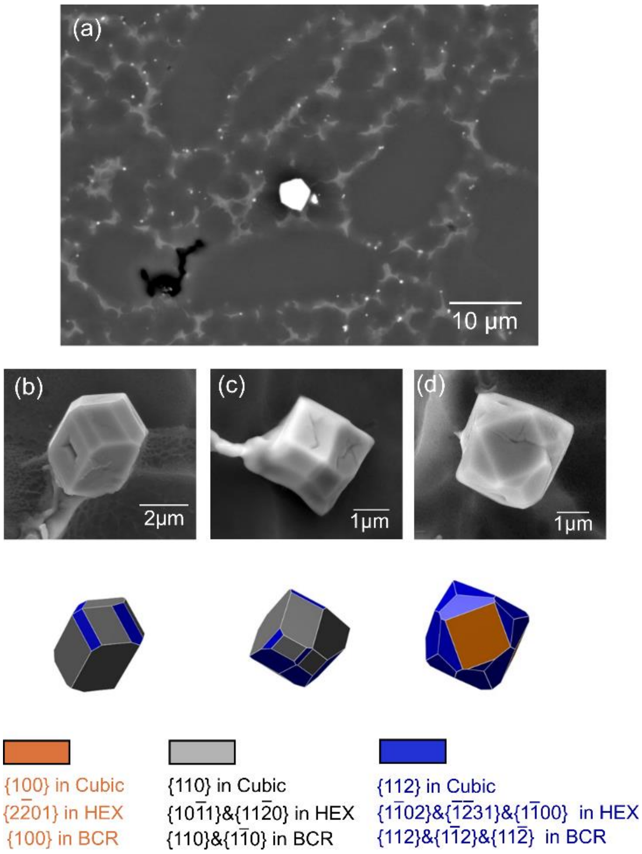

Figure 8: (a) a typical large Al_8Mn_5 particle in HPDC AZ91D. (b-d) SE-SEM images of three Al_8Mn_5 particles after selective etching of α-Mg, and polyhedron models based on {100}, {110}, {112} facets using a pseudo-cubic cell.

In our previous work at sand-casting cooling rates [35], we identified the Al_8Mn_5 growth facets using combined FIB-EBSD techniques as combinations of {100}, {110} and {112} using a pseudo-cubic (pc) BCR unit cell. To explore whether the larger Al_8Mn_5 particles in these HPDC samples had similar growth facets, deep etched images of Al_8Mn_5 particles were explored using polyhedron models. It was found that the deep etched images could usually be recreated from combinations of $\{100\}_{pc}$, $\{110\}_{pc}$ and $\{112\}_{pc}$ facets. Three such examples are shown in Figure 8(b)-(d) where the models were generated by plotting the {100}, {110} and {112} cubic facet families, and tuning the distance from the centroid to each facet to best match the deep etched SEM images. Thus, the larger Al_8Mn_5 particles in HPDC AZ91D have similar facets to sand cast AZ91 [35].

The wide range of polyhedral Al_8Mn_5 forms based on different combinations of the facet families indicates that these growth facets are sensitive to the local solidification conditions (thermal, solutal and/or kinetic) which are expected to vary substantially with time and location in the HPDC process. No simple trend of the polyhedral form of Al_8Mn_5 versus location in the HPDC part was identified in this work.

3.5 3D size distributions of Al_8Mn_5 particles

Figure 9(a) shows typical 3D rendered images of Al_8Mn_5 particles from FIB tomography with a 50nm slice step size. Each volume is ~13x13x13 μm^3 and comes from one of three locations: the casting centre, the porosity band, and the skin. Figure 9 (b) show histograms of the Al_8Mn_5 particle size distribution at each location. The histograms contain data from multiple tomograms as summarised in Table 2. The size distributions are plotted in terms of the number of Al_8Mn_5 particles and in terms of the volume occupied by the Al_8Mn_5 particles, separately. Two definitions of Al_8Mn_5 particle size are used: the equivalent sphere diameter and the "3D length". The latter is defined as the longest Feret diameter. Note in Figure 9(a) that the rendering causes the Al_8Mn_5 particles to appear rounded, but the particles are actually faceted as can be seen in the typical images from FIB sectioning shown as insets in the histograms of Figure 9(b). The volume fraction of Al-Mn IMCs varied from 0.11-0.22 vol. % depending on the location (Table 2). This is similar to the 0.10 vol.% calculated with Thermo-Calc TCMG4.0 [27] for the composition in Table 1, and 0.18% measured by Wang et al. [46] for HPDC AZ91D, which shows that a sufficient volume of material has been sampled and the thresholding approach was reasonable. The particle size results in Figure 9 are in general agreement with past work using TEM on small volumes. For example, Wei et al. [18] reported that Al-Mn particles were 100 nm to ~ lμm and usually less than 500 nm in AM and AZ Mg HPDC parts, and Wang et al. [19] reported Al_8Mn_5 to have polygonal morphology with size about 100 - 200 nm in HPDC AZ91D.

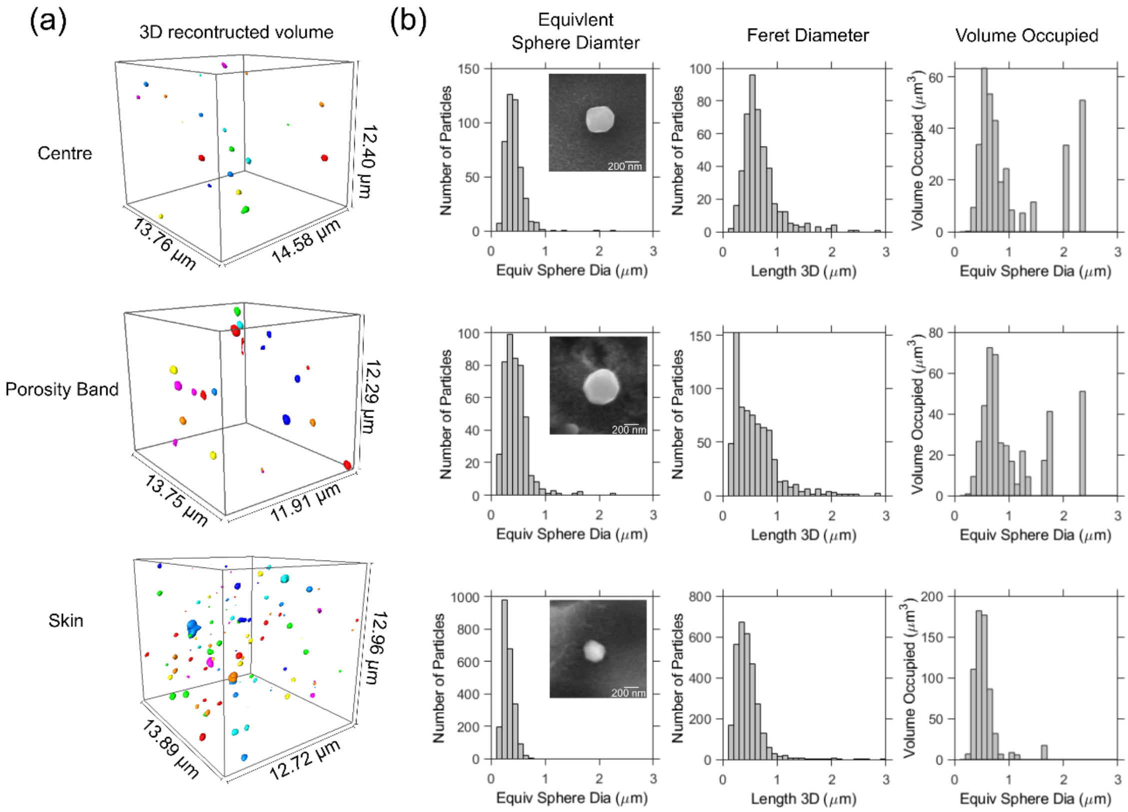

Figure 9: Al_8Mn_5 particle size data in different locations in the HPDC cross-section based on FIB-tomography. (a) Rendered images of Al_8Mn_5 particles in volumes of ~13x13x13 μm^3. Each particle has a unique colour. (b) Al_8Mn_5 particle size histograms in terms of the number of particles and the volume occupied by particles. The inset micrographs are typical 2D SEM images of Al_8Mn_5 particles in each location. The scale bar is 200nm in each case.

Table 2: Summary of the Al_8Mn_5 particle size data at different locations in HPDC AZ91D extracted from the distributions in Figs. 9 and 10 from FIB-tomography. ESD= equivalent sphere diameter. IMC= intermetallic compound. (ESD>180nm particles calculated)

		Center	Band	Skin
Distance from surface	[μm]	2700-2900	1500-1600	10-20
Number of tomograms	[-]	6	3	4
Total volume sampled	[μm^3]	24726	40203	25660

Number of IMCs measured	[-]	449	451	6547
Mean ESD	[nm]	432	453	163
Median ESD	[nm]	408	421	99.2
Standard deviation in ESD	[nm]	189	219	133
Maximum ESD	[nm]	2245	2245	1534
Volume of all Al-Mn IMCs	[μm^3]	35.9	44.3	55.8
Number density of particles	[μm^{-3}]	0.0182	0.0112	0.2551
Volume Fraction of IMCs	[-]	0.0015	0.0011	0.0022

The distributions are analysed in more detail in Figure 10 and summarised in Table 2. Figure 10(a) are box plots showing the median, the 25th percentile and 75th percentile, and a significant tail at large size in each particle population. Note that the largest Al_8Mn_5 particle in Figure 10(a) and Table 2 is less than 2.3μm, which is significantly smaller than the Al_8Mn_5 particle in Figure 5(b), 6(a) and 8(a) (>4μm), so the tail to large size extends to even larger size than in Figure 10(a), even though the randomly-selected regions only contained particles up to ~2.3μm.

The particle size distribution data were compared with various distributions including normal, lognormal and Weibull using probability test plots. At each location, the data were best described by a lognormal distribution as shown in Figure 10(b). This is consistent with many past studies that have shown grain size and particle size distributions are often well-described by a lognormal distribution (e.g. [3,47]) including Fe-bearing IMCs in cast aluminium alloys [48,49]. In Figure 10(b), there is a negative deviation from the lognormal test line at large particle size and at small particle size. At small size (<~200nm) this might be, at least partly, due to measurement uncertainty caused by the 50nm FIB slice distance. At large particle size (>~1 μm at a cumulative probability >~99%), the negative deviation from the straight line corresponds to Al_8Mn_5 particles larger than expected of this lognormal population. The presence of this small number of abnormally large grains in the populations can also be seen in the volume occupied histograms in Figure 9(a), especially at the casting centre and near the defect band. From this, and the observation of many abnormally large Al_8Mn_5 particles such as that in Figure 8(a), it can be concluded that the larger Al_8Mn_5 particles do not belong to the same population as the main lognormal distribution. The largest Al_8Mn_5 particles were very likely present in the shot chamber but there may also be other size populations associated with the different cooling rate and flow regimes in the different stages of HPDC: in the shot sleeve, the slow shot stage, the filling stage, and the intensification stage.

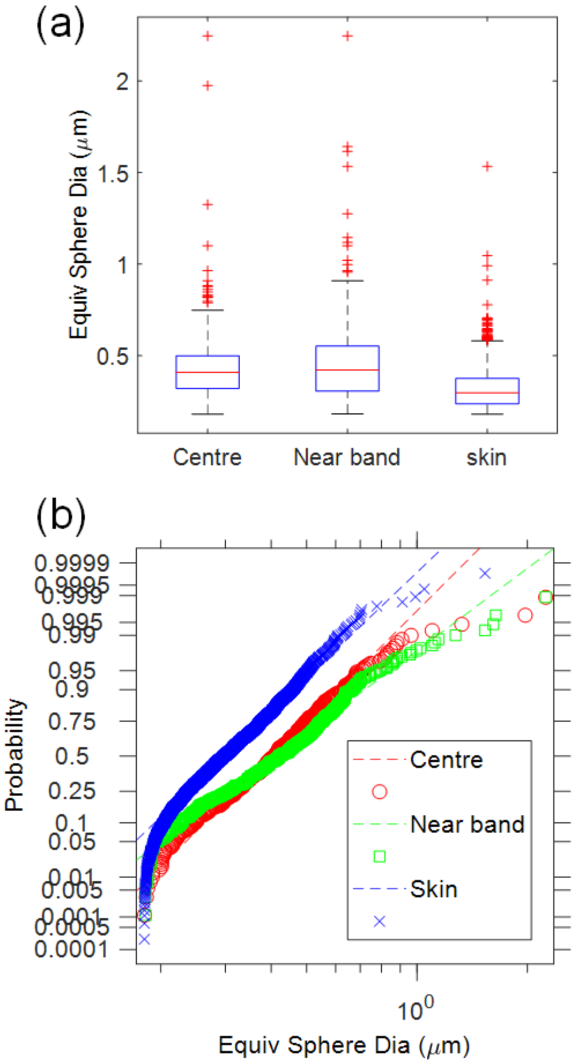

Figure 10: Analysis of the Al_8Mn_5 particle size data from FIB-tomography in Fig. 9 and Table 2. (a) Box plots showing the median, the 25th and 75th percentiles, and the outliers at large size. (b) lognormal probability plot to test for lognormality of the datasets at each location.

Considering now the distributions of Al_8Mn_5 particles in the three locations in the casting, it can be seen in Figures 9 and 10 and Table 2, that the Al_8Mn_5 size distributions were similar in the centre and defect band regions. For example, the size distributions from the centre and defect band overlap over most of the range from 1%-99% of the cumulative frequency plot in Figure 10(b), and the median Al_8Mn_5 size was similar (at 414 ±7 nm) (Table 2). Additionally, the tail at large size was similar in the centre and defect band, as can be seen in the volume occupied histograms in Figure 9(a), and the similar maximum Al_8Mn_5 particle size in the sampled volumes in Table 2. Thus, it is likely that the Al_8Mn_5 particle size distributions are similar throughout the interior regions of the castings.

In contrast, the Al_8Mn_5 size distribution was markedly different in the skin with significantly smaller and more numerous Al_8Mn_5 particles. For example, the Al_8Mn_5 distribution from the skin is shifted to smaller size (to the left) in Figure 10(b) and the median size is smaller by a factor of >4 in Table 2. There was also an order of magnitude higher number density (number per unit volume) of Al_8Mn_5 particles in the skin than in interior regions. This is shown in Table 2 and can be seen by eye in the rendered images in Figure 9(a). This higher number density is not simply due to the smaller Al_8Mn_5 size, but also because the volume fraction of Al_8Mn_5 particles was higher in the skin by a factor of 1.5-2 (Table 2).

Although a large number of Al-Mn particles were sampled by FIB tomography in this work (at least 449 in each region, Table 2), this technique is inherently limited by its small sampling volume. To partially offset this issue, within each type of region (the skin, band or centre), we selected each tomogram from different parts of the bar and sampled 3-6 tomograms (Table 2). For example, 4 tomograms were taken from randomly selected different parts of the skin, and all showed a higher volume fraction and smaller size of Al_8Mn_5 than the other two regions. Thus, the results in Figures 9 and 10 and Table 2 are likely to be generally valid across the whole bar. Figure 3 showed large variation in porosity distribution from sample to sample. From 2D backscatter electron imaging, there did not appear to be similarly large differences in the distributions of intermetallic compounds. However, further detailed FIB tomography work would be required to obtain quantitative detail on the variation in particle size distributions from sample to sample. Note that the most common porosity distribution in the HPDC bars was similar to Figure 3(b), and we performed our FIB slice and view characterisation and quantification on this type of sample.

3.6 Correlations between Al_8Mn_5 particles and $Mg_{17}Al_{12}$

In Figure 8(a), many bright Al_8Mn_5 particles appear close to eutectic regions on the 2D section. Therefore, the 3D FIB-tomography datasets were further explored to investigate any correlation between Al_8Mn_5 particles and eutectic $Mg_{17}Al_{12}$, noting from Figure 1 that Al_8Mn_5 forms before $Mg_{17}Al_{12}$.

In a previous FIB-tomography study on HPDC AZ91 [5], the eutectic $Mg_{17}Al_{12}$ was shown to form an interconnected scaffold-like network in 3D. The eutectic $Mg_{17}Al_{12}$ network was more profusely interconnected near the casting surface than at the casting centre which was attributed to the higher fraction of large ESCs near the centre resulting in a larger length scale of the $Mg_{17}Al_{12}$ network in the centre. A similar 3D $Mg_{17}Al_{12}$ microstructure was measured by FIB tomography in this work as shown in Figure 11. The $Mg_{17}Al_{12}$ (rendered in grey) forms a percolating network that is more intricately interconnected in the skin than in the defect band and centre.

In Figure 11 the Al_8Mn_5 particles are rendered with colour, where a different colour has been assigned to each distinct particle. It can be seen that some Al_8Mn_5 are in contact with $Mg_{17}Al_{12}$ and many are a significant distance away from $Mg_{17}Al_{12}$. Noting that the transparent phase is α-Mg, the numerous Al_8Mn_5 particles that are away from $Mg_{17}Al_{12}$ are fully surrounded by α-Mg in 3D. For those Al_8Mn_5 particles that share an interface with $Mg_{17}Al_{12}$, it is not possible with the techniques used to conclude whether $Mg_{17}Al_{12}$ nucleates on these pre-existing Al_8Mn_5 or whether Al_8Mn_5 particles are just pushed by the growth of α-Mg dendrites to the last liquid to solidify where they came into contact with $Mg_{17}Al_{12}$ during the final eutectic solidification. Further work is required to distinguish between these possibilities. A key finding from Figure 11 is that most Al_8Mn_5 particles do not contact $Mg_{17}Al_{12}$ in 3D.

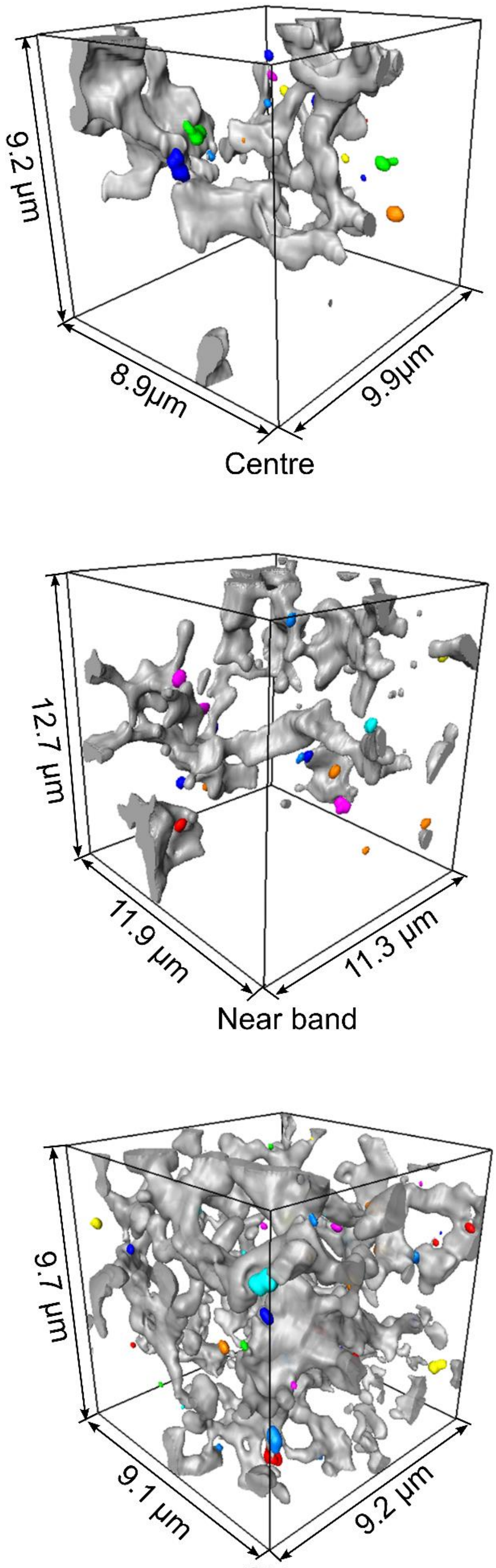

Figure 11. Rendered $Mg_{17}Al_{12}$ eutectic (grey) and Al_8Mn_5 (colours) from the FIB-tomography datasets in Figure. 9.

Comparing this HPDC study with past work at a controlled cooling rate of ~1 K s^{-1} [35], it can be concluded that the growth crystallography and twinning of larger Al_8Mn_5 particles in HPDC (Figure 6) is similar to slow cooled samples. However, the HPDC process generated a much wider variation in Al_8Mn_5 size distribution, number density, and morphology due to the wide range of cooling and flow conditions in the different stages of HPDC. This work has also identified significant differences in the Al_8Mn_5 size distribution in the skin and interior regions. The smaller particles, higher volume fraction and smaller interparticle spacing of Al_8Mn_5 particles in the skin region may partially contribute to the increased hardness reported in the skin [16]. In contrast, partial solidification in the shot sleeve ties up Mn in larger Al_8Mn_5 ESCs which will reduce the number density of Al_8Mn_5 particles and reduce the potential benefits that might be gained from smaller, more numerous particles.

4 Conclusions

Al-Mn intermetallic compounds have been characterised and quantified in high pressure die cast (HPDC) AZ91D test bars to understand the types of Al-Mn phases present, their faceted growth crystallography, and their size distribution in relation to the other phases and the key microstructural features in HPDC: the skin, the defect band, and $Mg_{17}Al_{12}$. The following conclusion can be drawn.

- Similar to Al_8Mn_5 particles in slow cooled (~1 K/s) AZ91D samples studied previously [35], Al_8Mn_5 particles in HPDC were often cyclic twins containing four orientations with $\{100\}_{BCR}$ twin planes. The facet morphology of large polyhedral Al_8Mn_5 particles could be described by combinations of {100}, {110}, and {112} facets.
- Al_8Mn_5 particles had a wide range of sizes and morphologies within the same HPDC component, but all could be broadly classified as equiaxed-polyhedral or complex-branched.
- The great majority of Al_8Mn_5 particles were sub-micrometre in size but there was a significant population of much larger (~5 μm) polyhedral particles whose size is similar to Al_8Mn_5 particles solidified at low cooling rate (1-3 K/s). These particles are concluded to be externally solidified crystals (ESCs) that nucleated and grew in the shot chamber analogous to the αMg ESCs.
- In all locations of the casting, the Al_8Mn_5 particle size distributions were reasonably well-described by lognormal distributions, accounting for the presence of an additional population(s) of larger grains associated with Al_8Mn_5 ESCs from the shot chamber.
- There were significant differences in the Al_8Mn_5 particle size and number density in the centre compared with the HPDC skin. The skin region had a median Al_8Mn_5 particle size (equivalent sphere diameter) of 99 nm, whereas the centre had a median Al_8Mn_5 size of 408 nm. The skin contained an order of magnitude higher number of Al_8Mn_5 particles per unit volume than interior regions
- 3D imaging showed that some Al_8Mn_5 particles were in contact with eutectic $Mg_{17}Al_{12}$ but the majority of Al_8Mn_5 particles were surrounded by α-Mg.
- This study has shown that HPDC of AZ91D generates numerous Al_8Mn_5 particles with diameter 100-400nm and a small interparticle spacing. Partial solidification in the

shot sleeve ties up Mn in larger Al_8Mn_5 ESCs which reduces the number density of Al_8Mn_5 particles.

Acknowledgements

Financial support from EPSRC (UK) under grant number EP/N007638/1 (the Future LiME Hub) is gratefully acknowledged. This work was partly supported by the National Natural Science Foundation of China (51904352). The authors acknowledge use of characterisation facilities within the Harvey Flower Electron Microscopy Suite, Department of Materials, Imperial College London.

References:

1 X. Li, S.M. Xiong, and Z. Guo: *J. Mater. Process. Technol.*, 2016, vol. 231, pp. 1–7.

2 A. Luo and A. Sachdev: *Int. J. Met.*, 2010, vol. 4, pp. 51–9.

3 A. Bowles, K. Nogita, M. Dargusch, C. Davidson, and J. Griffiths: *Mater. Trans.*, 2005, vol. 45, pp. 3114–9.

4 S. Biswas, F. Sket, M. Chiumenti, I. Gutiérrez-Urrutia, J.M. Molina-Aldareguía, and M.T. Pérez-Prado: *Metall. Mater. Trans. A Phys. Metall. Mater. Sci.*, 2013, vol. 44, pp. 4391–403.

5 A. V. Nagasekhar, C.H. Cáceres, and C. Kong: *Mater. Charact.*, 2010, vol. 61, pp. 1035–42.

6 B. Zhang, A. V. Nagasekhar, T. Sivarupan, and C.H. Caceres: *Adv. Eng. Mater.*, 2013, vol. 15, pp. 1059–67.

7 P. Sharifi, J. Jamali, K. Sadayappan, and J.T. Wood: *J. Mater. Sci. Technol.*, 2018, vol. 34, pp. 324–34.

8 K.V. Yang, M.A. Easton, and C.H. Cáceres: *Mater. Sci. Eng. A*, 2013, vol. 580, pp. 191–5.

9 S. Barbagallo, H.I. Laukli, O. Lohne, and E. Cerri: *J. Alloys Compd.*, 2004, vol. 378, pp. 226–32.

10 D.G.L. Prakash and D. Regener: *J. Alloys Compd.*, 2008, vol. 461, pp. 139–46.

11 C.M. Gourlay and A.K. Dahle: *Nature*, DOI:10.1038/nature05426.

12 P. Sharifi, J. Jamali, K. Sadayappan, and J.T. Wood: *Metall. Mater. Trans. A*, DOI:10.1007/s11661-018-4633-0.

13 H. Cao and M. Wessén: *Int. J. Cast Met. Res.*, 2005, 18, vol. 18.

14 X. Li, S.M. Xiong, and Z. Guo: *Mater. Sci. Eng. A*, 2015, vol. 633, pp. 35–41.

15 C.M. Gourlay, H.I. Laukli, and A.K. Dahle: *Metall. Mater. Trans. A*, 2007, vol. 38, pp. 1833–44.

16 C.H. Cáceres, J.R. Griffiths, A.R. Pakdel, and C.J. Davidson: *Mater. Sci. Eng. A*, 2005, vol. 402, pp. 258–68.

17 E. Deda, T.D. Berman, and J.E. Allison: *Metall. Mater. Trans. A*, 2017, vol. 48, pp. 1999–2014.

18 L.-Y. Wei, H. Westengen, T.K. Aune, and D. Albright: *Magnes. Technol. 2000*, 2013, pp. 153–60.

19 R.M. Wang, A. Eliezer, and E. Gutman: *Mater. Sci. Eng. A*, 2003, vol. 344, pp. 279–87.

20 G. Zeng, X. Zhu, S. Ji, and C.M. Gourlay: *Magnesium Technology 2018*, pp.137-144. Springer, Cham, 2018

21 V.Y. Gertsman, J. Li, S. Xu, J.P. Thomson, and M. Sahoo: *Metall. Mater. Trans. A Phys. Metall. Mater. Sci.*, 2005, vol. 36, pp. 1989–97.

22 O. Lunder, K. Nişanciogu, and R.S. Hansen: *SAE Tech. Pap.*, 1993, pp. 117–26.

23 M. Liu and G.-L. Song: *Corros. Sci.*, 2013, vol. 77, pp. 143–50.

24 M. Lugo, M.A. Tschopp, J.B. Jordon, and M.F. Horstemeyer: *Scr. Mater.*, 2011, vol. 64, pp. 912–5.

25 Y. Uematsu, K. Tokaji, and M. Matsumoto: *Mater. Sci. Eng. A*, 2009, vol. 517, pp. 138–45.

26 ASTM B94: *Annu. B. ASTM Stand.*, 2018, pp. 1–6.

27 Thermo-Calc software: 2019.

28 G. Zeng, K. Nogita, S. Belyakov, J.W. Xian, S.D. McDonald, K. V. Yang, H. Yasuda, and C.M. Gourlay. *Magnesium Technology 2017*, pp. 597-603. Springer, Cham, 2017.

29 L. Peng, G. Zeng, T.C. Su, H. Yasuda, K. Nogita, and C.M. Gourlay: *Jom*, 2019, vol. 71, pp. 2235–44.

30 C.P. Corby, N.J. Ricketts, M. Qian, and R.D. Bailey: *Magnes. Technol. 2004*, 2004, pp. 209–14.

31 C. Bi, S. Xiong, X. Li, and Z. Guo: *Metall. Mater. Trans. B*, 2016, vol. 47, pp. 939–47.

32 L. Wang, T. Nguyen, G. Savage, and C. Davidson: in *International Journal of Cast Metals Research*, vol. 16, 2003, pp. 409–17.

33 H.I. Laukli, A. Graciotti, O. Lohne, H. Gjestland, and S. Sannes: in *NADCA Transactions*, 2002, pp. T02-035, pp.1–4.

34 J. Song, S.M. Xiong, M. Li, and J. Allison: *J. Alloys Compd.*, 2009, vol. 477, pp. 863–9.

35 G. Zeng, J.W. Xian, and C.M. Gourlay: *Acta Mater.*, 2018, vol. 153, pp. 364–76.

36 F. Bachmann, R. Hielscher, and H. Schaeben: *Solid State Phenom.*, 2010, vol. 160, pp. 63–8.

37 Z. Fan, G. Liu, and Y. Wang: *J. Mater. Sci.*, 2006, vol. 41, pp. 3631–44.

38 Y. Du, J. Wang, J. Zhao, J.C. Schuster, F. Weitzer, R. Schmid-Fetzer, M. Ohno, H. Xu, Z.K. Liu, S. Shang, and W. Zhang: *Int. J. Mater. Res.*, 2007, vol. 98, pp. 855–71.

39 R. Sarvesha, W. Alam, A. Gokhale, T.S. Guruprasad, S. Bhagavath, S. Karagadde, J. Jain, and S.S. Singh: *Mater. Sci. Eng. A*, 2019, vol. 759, pp. 368–79.

40 M. Ellner: *Metall. Trans. A*, 1990, vol. 21, pp. 1669–72.

41 S. Thimmaiah, Z. Tener, T.N. Lamichhane, P.C. Canfield, and G.J. Miller: *Zeitschrift fur Krist. - Cryst. Mater.*, 2017, vol. 232, pp. 601–10.

42 S. Balanetskyy, D. Pavlyuchkov, T. Velikanova, and B. Grushko: *J. Alloys Compd.*, 2015, vol. 619, pp. 211–20.

43 S. Yao, S. Liu, G. Zeng, X. Li, T. Lei, Y. Li, and Y. Du: *Metals (Basel).*, 2019, vol. 9, p. 460.

44 K. Yoshida, T. Yamamoto, and S. Nagata: *Jpn. J. Appl. Phys.*, 1974, vol. 13, pp. 400–10.

45 S. Lun Sin, D. Dubé, and R. Tremblay: *Mater. Charact.*, 2007, vol. 58, pp. 989–96.

46 M.Y. Wang, J.J. Williams, L. Jiang, F. De Carlo, T. Jing, and N. Chawla: *Metallogr. Microstruct. Anal.*, 2012, vol. 1, pp. 7–13.

47 T. Kubo, Y. Wakashima, H. Imahashi, and M. Nagai: *J. Nucl. Mater.*, 1986, vol. 138, pp. 256–67.

48 G. Timelli and F. Bonollo: *Mater. Sci. Eng. A*, 2010, vol. 528, pp. 273–82.

49 B.G. Dietrich, H. Becker, M. Smolka, A. Keßler, A. Leineweber, and G. Wolf: *Adv. Eng. Mater.*, 2017, vol. 19, p. 1700161.